The Influence of Changing Orbital Parameters and Surface Boundary Conditions on Climate Simulations for the Past 18 000 Years

JOHN E. KUTZBACH AND PETER J. GUETTER

Center for Climatic Research, University of Wisconsin–Madison, Madison, Wisconsin, 53706

(Manuscript received 16 September 1985, in final form 20 February 1986)

ABSTRACT

General circulation model experiments at 3000-year intervals for the past 18 000 years were made to estimate the magnitude, timing, and pattern of the climatic response to prescribed changes of orbital parameters (date of perihelion, axial tilt, eccentricity) and glacial-age lower boundary conditions (ice sheets, land albedo, sea ice and sea surface temperature). The experiments used the Community Climate Model (CCM) of the National Center for Atmospheric Research (NCAR). The response of monsoon circulations and tropical precipitation to the orbitally produced solar radiation changes was much larger than the response to changes of glacial-age boundary conditions. The continental interior of Eurasia was 2–4 K warmer in summer, and summer monsoon precipitation of North Africa–South Asia was increased by 10–20% between 12 000 and 6000 yr BP (before present) when perihelion occurred during northern summer (rather than in winter as now) and the earth's axial tilt was larger than now. Southern Hemisphere summer monsoons were weaker during the same period. In northern midlatitudes, glacial-age features such as the North American ice sheet exerted a strong influence on the climate until 9000 yr BP. Much of the climatic change of the period 12 000 to 6000 yr BP can be described as an amplified (weakened) seasonal cycle in response to the larger (smaller) seasonal radiation extremes of the Northern (Southern) Hemisphere. Summers were warmer and winters colder in Northern Hemisphere lands, but there was little change in annual average temperature. However, because of the nonlinear relationship between saturation vapor pressure and temperature, the sensitivity of the hydrologic cycle to orbital parameter changes was larger in summer than in winter (and in the tropics rather than high latitudes); in the northern tropics, this led to a net increase in estimated annual average precipitation and precipitation minus evaporation. Many features of the results are in agreement with geologic evidence.

1. Introduction

During the past 18 000 years, the climate changed from full glacial to interglacial conditions. Because these climatic changes were large, and because the geologic evidence is widespread and well dated from radiocarbon, this 18 000-year record of climatic change is ideal for comparisons with climates simulated by climate models. At the last glacial maximum, around 18 kyr BP (1000 yr before present), large ice sheets covered parts of North America and Europe, sea ice in both hemispheres extended 10° latitude or more further equatorward than it does now, ocean temperature was generally lower, boreal treeless and coniferous vegetation covered much of the continents in mid-latitudes, and tropical lands were more arid than now (CLIMAP, 1976, 1981; Peterson et al., 1979). Rapid deglaciation took place between about 15 and 12 kyr BP, and, by about 9 kyr BP, the Wisconsin ice sheets disappeared (except in eastern North America), and sea level and sea surface temperature approached present conditions. Many aspects of the rapid deglaciation, including its timing, mechanisms, and regional expressions, are summarized by Ruddiman and Duplessy (1985). In northern midlatitudes, the period around 9–6 kyr BP was generally warmer and drier than present, but since 6 kyr BP, the climate has become cooler and moister (Wright, 1971; Webb et al., 1983). From about 12 to 5 kyr BP, tropical lake levels were high; this "pluvial" interval in the tropics contrasted with the more arid conditions before and after (Street and Grove, 1979; Street-Perrot and Roberts, 1983). Also, marine sediment cores located near the margins of the monsoon lands of North Africa–South Asia record evidence of this period of strengthened monsoons (Prell, 1978, 1984).

Observational studies (Hays et al., 1976; Ruddiman and McIntyre, 1981) and experiments with simplified climate models representing global-average or zonal-average conditions (Milankovitch, 1941; Suarez and Held, 1976; Berger, 1978; Schneider and Thompson, 1979; Imbrie and Imbrie, 1980; Birchfield et al., 1981) have shown that changes in the latitudinal and seasonal distribution of solar radiation, produced by orbital parameter changes, could be the primary cause of glacial–interglacial fluctuations over hundreds of thousands of years. The orbital variations involve a) precession of the earth's axis which moves the date of perihelion (period of about 22 000 years); b) changes in the tilt of the earth's axis (period of about 41 000 years); and c)

changes in the eccentricity of the orbit (period of about 100 000 years). The details of the processes, however, that link the solar radiation changes to climatic changes are not well known.

Atmospheric general circulation models (AGCMs) can be used to study the spatial patterns of atmospheric response to orbital parameter changes in order to understand some of the mechanisms whereby the solar radiation changes produce large climatic changes. In this manner, experiments with AGCMs can complement the studies with more highly parameterized models. AGCM experiments by Mitchell (1977) simulated high latitude warming of northern continents in summer with orbital parameters set to 10 kyr BP values. Subsequent experiments with AGCMs (Kutzbach, 1981; Kutzbach and Otto-Bliesner, 1982; Kutzbach and Guetter, 1984a,b) simulated warmer summers and colder winters and stronger summer and winter monsoons in the Northern Hemisphere with the earth's orbital parameters set to 9 kyr BP values. These results were consistent with Prell's (1978, 1984) findings from ocean sediment cores that indicators of summer monsoon intensity show a concentration of variance at periods of the precession cycle (about 22 000 years).

Several previous AGCM experiments for 18 kyr BP have shown the importance of glacial-age lower boundary conditions for influencing the atmospheric circulation: Alyea (1972), Williams et al. (1974), Gates (1976a,b) and Manabe and Hahn (1977). The experiments by Gates and Manabe and Hahn used boundary conditions for August of 18 kyr BP produced by CLIMAP Project Members (1976). Both August and February 18 kyr BP boundary conditions (CLIMAP Project Members, 1981) have been used by Hansen et al. (1984), Kutzbach and Guetter (1984a), and Rind and Peteet (1985) in AGCM experiments; Manabe and Broccoli (1985) coupled an AGCM to a simple model of the mixed-layer ocean to study the influence of the 18 kyr BP ice sheet on the simulated atmosphere/ocean climate.

The purpose of this paper is to present an overview of fourteen AGCM simulation experiments with the National Center for Atmospheric Research (NCAR) Community Climate Model (CCM) for 18, 15, 12, 9, 6, 3 and 0 kyr BP. We use the magnitude, timing and spatial structure of the climatic response to changes of orbital parameters and lower boundary conditions over the 18 000-year period to a) identify some of the physical mechanisms that produced large climatic changes during this interval, and b) assess the relative importance of the changes of orbital parameters and the long time-constant glacial-age features, such as land-ice, in the evolution of the climate over this 18 000-year period. Moreover, determining the model's sensitivity to a different seasonal radiation cycle, such as that of 9 kyr BP, helps us to identify the continent-scale monsoonal response to the seasonality of radiation just as other sensitivity experiments have helped to elucidate the climatic role of such factors as mountains, snow cover, and sea surface temperature.

Each of the fourteen AGCM experiments (seven periods separated by 3000-year intervals, and two seasons per period) is a "snapshot" view of the general circulation for specified orbital parameter and lower boundary conditions. We assume that changes in the latitudinal and seasonal distribution of solar radiation, associated with orbital parameter changes, were ultimately responsible for the wastage of the large continental ice sheets and the warming of the ocean (Hays et al., 1976; Imbrie and Imbrie, 1980). However, these lower boundary conditions are not simulated explicitly. Rather, lower boundary conditions for glacial ice, sea-ice, ocean surface temperature, and land albedo are adjusted for each 3000-year interval in a manner consistent with the geologic evidence. Simultaneously, the solar radiation is calculated at each 3000-year interval from the orbital parameters of axial tilt, eccentricity, and position of perihelion (Table 2). In one experiment (18 kyr BP), the atmospheric concentration of carbon dioxide is set at 200 ppmv rather than at 330 ppmv, the control case value. Even though current computer resources have not permitted us to make simulation experiments with an interactive (coupled) dynamical-ocean–atmosphere model, this is our long-term goal. [See Appendix (part 3).]

The simulations are sensitivity experiments to various combinations of external and lower boundary conditions (Fig. 1). The 18 kyr BP solar radiation regime is similar to that of 0 kyr BP, and therefore the 18 kyr BP experiment tests primarily the atmospheric adjustment to glacial-age boundary conditions. The experiments for 9, 6 and 3 kyr BP illustrate primarily the atmospheric response to changes in seasonality of solar radiation because the lower boundary conditions are those of today (except for a small North American ice sheet at 9 kyr BP). At 15 and 12 kyr BP, both radiation and lower boundary conditions changes are large.

This modeling study is part of the Cooperative Holocene Mapping Project (COHMAP) which is producing global maps of paleoclimatic conditions for the past 18 000 years at 3000-year intervals and comparing the observed paleoclimates and the simulated climates. A knowledge of how well general circulation models simulate past climates provides one measure of their ability to estimate future climates. A series of papers focusing on regional details of the simulated climate and the paleoclimatic record are completed or planned: Peterson et al. (1979), Webb et al. (1985), Kutzbach and Wright (1986), Kutzbach and Street-Perrott (1985).

Section 2 reviews previous results of sensitivity experiments with altered orbital parameter and glacial boundary conditions; this is followed by a description of the model, boundary conditions, and experimental procedures in section 3. The results are in section 4

and conclusions in section 5. An appendix describes other paleoclimatic experiments, planned or in progress, involving models with variable soil moisture, a coupled mixed-layer ocean, and changed concentrations of CO_2 and aerosol.

2. General response of the circulation to orbital parameter changes and glacial-age lower boundary conditions

Certain general features of the climatic response to changes of orbital parameters and glacial-age boundary conditions can be anticipated from the results of previous AGCM experiments.

a. *Orbital parameter changes*

The seasonal cycle of solar radiation was amplified considerably in the Northern Hemisphere between about 15 and 6 kyr BP (compared to present) because perihelion occurred in the northern summer half-year (it is now in northern winter) and because the earth's axis was tilted almost 1° more than today (Milankovitch, 1941; Berger, 1978). At the time of maximum amplification of the seasonal cycle, about 9 kyr BP, Northern Hemisphere insolation was more than 35 W m^{-2} (8%) greater than today in July and about 20 W m^{-2} (−8%) less in January.

These changes in seasonal solar radiation are large compared to the forcing perturbations typically used in AGCM sensitivity experiments; for example, a 1% change in the solar constant corresponds to a global average solar radiation change of about 3.4 W m^{-2} and a doubling of the atmospheric concentration of CO_2 corresponds to a 4 W m^{-2} increase in the radiative heating at the Earth's surface. (This estimate of 4 W m^{-2} includes certain direct radiative effects of tropospheric and surface heating but excludes the further amplification of the CO_2 effect associated with hydrologic cycle feedbacks; Ramanathan, 1981.) Based upon a simple global energy budget formula, the equilibrium response of global and annual average surface temperature to a 1% increase in the solar constant is about 1.5 K (Schneider and Mass, 1975). Of course, the radiation changes associated with orbital variations are largely seasonal rather than annual-mean perturbations, and, the simple formulation of the global-average surface temperature sensitivity quoted previously ignores important feedbacks such as would be associated with advection and the hydrologic cycle. Nevertheless, one can anticipate an increase in the amplitude of the seasonal cycle of land surface temperature of several degrees Kelvin for an 8% increase of the amplitude of the seasonal cycle of solar radiation (such as occurred in the Northern Hemisphere at 9 kyr BP).

Because the thermal properties of land and ocean are different, Northern Hemisphere continents and oceans will respond differently to the increased amplitude of the seasonal radiation cycle. For example, the amplification of the seasonal cycle of sea surface temperature for a 50 m mixed layer ocean would be less than about one-fifth that for the land surface.

From hydrostatic considerations, these large temperature changes over Northern Hemisphere land cause lower atmospheric pressure over land (and higher pressure over the oceans) in July of 9 kyr BP, with the opposite changes in January. Such changes are analogous to those of the present seasonal cycle; namely, there are large areas of low pressure over continents and high pressure over oceans during summer, and the reverse in winter. In other words, the amplified seasonal cycle of solar radiation in the Northern Hemisphere amplifies the normal seasonal (monsoonal) circulations and produces stronger summer and winter monsoons.

Experiments with AGCMs for the solar radiation conditions at 9 kyr BP showed this enhanced monsoonal response to changed orbital forcing and indicated substantial increases in precipitation and precipitation minus evaporation in the Northern Hemisphere tropics and subtropics around 9 kyr BP (Kutzbach, 1981; Kutzbach and Otto-Bliesner, 1982; Kutzbach, 1983; Kutzbach and Guetter, 1984a,b). In contrast, the Southern Hemisphere experienced reduced seasonality of solar radiation (compared to present) and weaker monsoons because perihelion was then in southern winter.

b. *Glacial-age lower boundary conditions*

The AGCM experiments of Gates (1976a,b) and Manabe and Hahn (1977), using glacial-age boundary conditions, simulated the global-average surface air temperature about 4–5 K below present values for July–August of 18 kyr BP. Consistent with the generally lower temperature, both models simulated a reduction in the intensity of the hydrologic cycle, i.e., less precipitation and less evaporation. For both models, the simulated decrease in temperature over land exceeded the prescribed decrease of ocean surface temperature. Moreover, the larger cooling of the land relative to the ocean tended, from hydrostatic considerations, to weaken the Northern Hemisphere summer monsoon circulations and, in general, to increase the flow of air from land to ocean.

3. Description of model, procedures, boundary conditions

a. *Model*

The simulation experiments were made with the Community Climate Model (CCM) of the National Center for Atmospheric Research (NCAR); see Pitcher et al. (1983) and Ramanathan et al. (1983) for a description of the model. The model incorporates atmospheric dynamics based upon the equations of fluid motion; it includes radiative and convective processes,

condensation, and evaporation. The surface energy budget and surface temperature are computed over land, ice sheets, and sea ice. Orographic influences of mountains (and ice sheets) are included. Orbital parameters (eccentricity, tilt, date of perihelion), atmospheric CO_2 concentration, sea surface temperature, sea-ice limit, snow cover, land albedo, and effective soil moisture are prescribed. For "perpetual" January and July simulations, orbital parameters are set to give the solar radiation appropriate for 16 January and 16 July. The solar constant is 1370 W m^{-2}. The model has nine vertical levels (sigma coordinates) and uses a spectral representation, to wavenumber 15 (rhomboidal), of the horizontal fields of wind, temperature, pressure and moisture. When needed for certain calculations, the spectral representation is converted to a grid of 4.4° latitude by 7.5° longitude.

One experiment for 9 kyr BP was made with a version of the CCM having a full seasonal cycle, variable soil moisture, and variable snow cover parameterizations (see Appendix).

b. *Procedures*

The experiments were started with all model variables set at values for day 400 of an NCAR CCM control simulation, but with the solar radiation and lower boundary conditions changed from modern to estimates of past values. In most experiments, the model was run for 450 simulated days. (See Table 1 for summary.) In the first 60 days, the model's circulation was adjusting to the changed boundary conditions, and these days were ignored. Three 90-day averages were obtained from the remaining model days (here numbering the days from the beginning of our experiments): days 61–150, 211–300, and 361–450. By removing the two 60-day segments (151–210 and 301–360), the three 90-day averages are assumed to be independent (Blackmon et al., 1983). The three 90-day segments were then averaged and compared to a similarly constructed ensemble-average control (modern) simulation. (The 450-day control simulation also started at day 400.) The six independent 90-day averages, three from each experiment and three from the control, were used to estimate the model's natural variability and assess the statistical significance of the simulated climatic changes (Chervin and Schneider, 1976).

While the fourteen AGCM experiments were "perpetual" January and July simulations, two additional experiments were annual cycle simulations for 9 kyr BP and 0 kyr BP (Kutzbach and Otto-Bliesner, 1982; Appendix). For these two annual cycle simulations, the annual-average precipitation, precipitation minus evaporation, and surface temperature, based upon the full annual cycle, were adequately approximated, in most regions, by the appropriately weighted averages of these variables for July and January. The weighting factors used were the lengths of the summer and winter half-years, T_s and T_w, measured from equinox to equinox, as defined by Vernekar (1972); see Table 1 herein. The modern values for T_s and T_w are 186.4 and 178.8 days, respectively; at 9 kyr BP the values were 179.3 and 186.0 days, respectively. The approximation of the annual average was least accurate in regions where a significant amount of precipitation occurred around the equinoxes; e.g., near the equator. We made use of this approximation to estimate certain annual-average conditions from the perpetual January and July results.

c. *Boundary conditions (summarized in Table 2)*

The boundary condition values for solar radiation, atmospheric composition, ice sheets, sea level, sea ice, sea surface temperature and land albedo are summarized below.

1) *External conditions—Solar radiation.* Changes in solar radiation depend upon the earth's axial tilt, ec-

TABLE 1. List of experiments and weighting factors.

kyr BP*	Perpetual January	Perpetual July	Annual cycle†	T_s#	T_s/365.24
0	×	×	×	186.4	(0.510)
3	×	×		185.8	(0.509)
6	×	×		182.7	(0.500)
9	×	×	×	179.3	(0.491)
9 (no land ice)		×		179.3	(0.491)
12	×	×		178.1	(0.488)
15	×	×		180.1	(0.493)
18	×	×		183.9	(0.504)
18 (CO_2 = 200 ppmv)	×	×		183.9	(0.504)

* The 0, 9 and 18 *kyr* BP experiments are 450 days in length for both July and January. The 3, 6, 12 and 15 *kyr* BP experiments are 450 days in length for January, and 150 days in length for July.

† "Annual cycle" refers to full annual cycle experiments with a version of the CCM with interactive soil moisture.

The weights used to estimate weighted annual-averages are T_s (the length of the summer half-year, vernal to autumnal equinox, in days) and $T_w = 365.24 - T_s$ such that:

$$(\ )_{\text{annual}} = [T_s \times (\ )_{\text{July}} + T_w \times (\ )_{\text{Jan}}] \div 365.24.$$

TABLE 2. Summary of boundary conditions.

Orbital parameters and atmospheric concentration of CO_2

Yr (*kyr* BP)	Eccentricity of orbit	Axial tilt (degrees)	Position of perihelion* (degrees)	CO_2 (ppmv)
0	0.0167	23.44	78	330
3	0.0178	23.82	128.9	330
6	0.0187	24.11	179.1	330
9	0.0193	24.24	228.8	330
12	0.0196	24.15	277.9	330
15	0.0196	23.87	327.0	330
18	0.0195	23.45	16.3	330 (and 200)

Surface boundary conditions (see text for details)

	Ice sheets	Sea level	SST	Sea ice	Land albedo
0	control	control	control	control	control
3	control	control	control	control	control
6	control	control	control	control	control
9	Fig. 2	−10 m	control	control	control
12	Fig. 2	−40 m	see text	Fig. 2, 10	see text
15	Fig. 2	−100 m	Fig. 5, 10	Fig. 2, 10	Fig. 2
18	Fig. 2	−100 m	Fig. 5, 10	Fig. 2, 10	Fig. 2

* Position of perihelion (degrees of celestial longitude) measured clockwise from the vernal equinox.

centricity of orbit, and longitude of perihelion (Berger, 1978). For July and January at 18 kyr BP, the radiation differences between 18 kyr BP and 0 kyr BP were less than 1% of modern values at all latitudes. Solar radiation was 3–4% more in March–May and 3–4% less in September–November when compared to the present because perihelion occurred near the vernal equinox at 18 kyr BP. After 18 kyr BP, the date of perihelion shifted toward the Northern Hemisphere summer solstice and the axial tilt increased. At 12 kyr BP, the perihelion occurred in June and, at 9 kyr BP, it was in late July. The axial tilt was 24.2° at 9 kyr BP, compared to 23.4° at 18 kyr BP and the present.

2) *Atmospheric conditions—carbon dioxide concentration, aerosol.* Evidence from ice cores (Oeschger et al., 1983; Lorius et al., 1984) indicates that atmospheric CO_2 concentration was about 200 ppmv at glacial maximum (around 18–15 kyr BP); it increased to about 265–275 ppmv by about 9 kyr BP where it remained until recently (Neftel et al., 1982; Lorius et al., 1984; Stuiver et al., 1984); Fig. 1. Our main series of experiments were made with the CO_2 concentration set at the control case value of 330 ppmv. However, the 18 kyr BP experiment was also run with a CO_2 concentration of 200 ppmv (see Appendix). We have not yet included the high tropospheric loadings of land and marine aerosols that were probably characteristic of glacial times (Kolla et al., 1979; Thompson and Mosley-Thompson, 1981; Petit et al., 1981). See Fig. 1 herein.

3) *Lower boundary conditions.* CLIMAP Project Members' (1981) estimates of boundary conditions for ice sheet location and height, sea ice location, and sea surface temperature were used for the 18 kyr BP experiment (Fig. 1, Fig. 2). CLIMAP boundary conditions are set nominally for February and August; however, we have applied these values to January and July. Values for the 4.4° latitude by 7.5° longitude grid of the NCAR CCM were obtained by averaging values from surrounding 2° squares of the CLIMAP grid. After 18 kyr BP, these CLIMAP boundary conditions were adjusted toward modern boundary conditions (Fig. 1) as summarized below.

• *Ice sheets, sea level, land.* At 18 kyr BP the North American ice sheet covers 77 model grid points and has a maximum elevation of about 3300 m over Hudson Bay; the European ice sheet covers 56 model grid points and has a maximum elevation of about 2700 m over Scandinavia. Parts of the west Antarctic ice sheet are about 500–1000 m higher than at present. The North American ice sheet is a much higher topographic barrier than the Rockies because the spectral representation of the orography smoothes the relatively "narrow" mountain ranges far more than it smoothes the broad ice sheet (Fig. 2). Consistent with the large ice sheets on the continents, sea level is about 100 m lower and certain ocean grid points in the control case are land grid points at 18 kyr BP; for example, between Alaska and Eastern Siberia, and in the Austral-Asian region (Fig. 2).

For the experiments after 18 kyr BP, we adjust the limits of the ice sheets following the analysis of Denton and Hughes (1981). At 15 kyr BP the ice limits are very close to those at 18 kyr BP, and they are kept identical in the model. At 12 kyr BP the area covered by ice is reduced in western North America and in western Europe (Fig. 2).

Even though the height of the ice sheets after 18 kyr BP is not well known, estimates of ice volume obtained from isotopic records in marine sediments (Ruddiman and McIntyre, 1981) suggest little change in ice volume between 18 and 15 kyr BP and rapid melting between 15 and 12 kyr BP. Thus, at 15 kyr BP we set ice sheet height equal to that of 18 kyr BP, but at 12 kyr BP we reduce the height by one-half. The combination of reduced height and decreased area of ice approximates an ice volume for 12 kyr BP of about 40% of glacial maximum. We also adjust sea level to a value 40 m below present. The maximum heights of the ice sheets at 12 kyr BP are 1650 m (North America) and 1300 m (Europe). The European ice sheet is gone at 9 kyr BP, (its actual boundaries occupied less than one model grid rectangle) and the North American ice sheet is reduced in size compared to 12 kyr BP (Fig. 2) and assigned a maximum height of 800 m. Sea level is 10 m lower than present. At 6 and 3 kyr BP there is no excess land ice and sea level is the same as at 0 kyr BP.

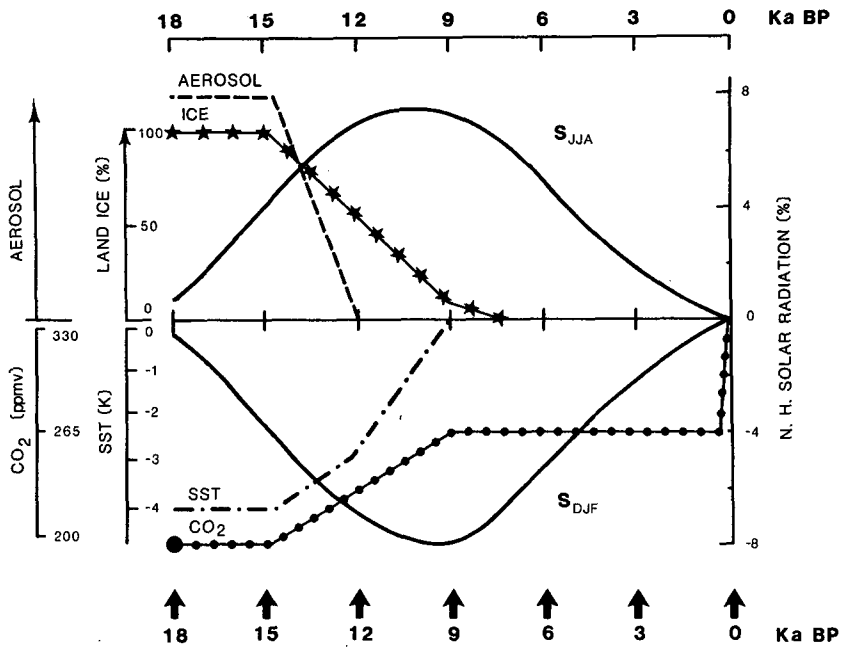

FIG. 1. Schematic diagram of major changes since 18 kyr BP in external forcing (Northern Hemisphere solar radiation in June–August (S_{JJA}) and December–February (S_{DJF}), as percent difference from present) and internal boundary conditions: land ice (ICE) as percent of 18 kyr BP ice volume (CLIMAP Project Members, 1981; Denton and Hughes, 1981); global mean-annual sea-surface temperature (SST), including calculated surface temperature over sea ice, as departure from present, *K* (CLIMAP Project Members, 1981); excess glacial-age aerosol (AEROSOL), arbitrary scale (Petit et al., 1981; Thompson and Mosley-Thompson, 1981); and atmospheric CO_2 concentration (CO_2), in ppmv (Neftel et al., 1982; Lorius et al., 1984). The arrows correspond to the seven sets of simulation experiments with the CCM. One experiment for 18 kyr BP included the lowered CO_2 concentration (200 ppmv, large solid circle); the main series of experiments used the same CO_2 concentration as the control case (330 ppmv) rather than the stepwise increase. Experiments incorporating the increased glacial-age aerosol loading are planned but not included here.

A small ice sheet still existed in Labrador at 6 kyr BP, but it would have occupied less than one model grid rectangle.

• *Sea ice.* The CLIMAP-specified sea-ice boundary for 18 kyr BP is shifted far south of its modern position in the North Atlantic in both January and July and north of its modern position in the southern oceans (Figs. 2, 5, 10). In the model experiments, sea ice is kept at the 18 kyr BP positions for 15 and 12 kyr BP; thereafter, it is placed at the modern position.

• *Sea surface temperature.* Major features of the charts produced by CLIMAP Project Members (1981) of sea surface temperature (SST) for 18 kyr BP are substantially colder sub-polar and middle latitude waters immediately equatorward of the expanded sea ice margin, colder equatorial waters, and little change in the position and temperatures of the central gyres in the subtropical Atlantic, Pacific, and Indian oceans. The CLIMAP-specified SSTs are used in the model experiments at both 18 and 15 kyr BP. (See Figs. 5 and 10 for January and July SST maps for 18 kyr BP.) The global-average SST was about 2 K lower than at present. At 12 kyr BP the SST anomalies are reduced to one-half of their 18 (15) kyr BP values everywhere except in the North Atlantic where SSTs were most likely kept low by the addition of melt water (Ruddiman and McIntyre, 1981); there, the SSTs are set at 18 (15) kyr BP values at all grids from 46.4°N northward. At 9 kyr BP and thereafter, SST's are set at 0 kyr BP values; this boundary condition is consistent with evidence from ocean sediment cores indicating that SST's were near modern values since about 9 kyr BP, except perhaps near coastlines where changes in upwelling occurred (Ruddiman and Mix; Prell, personal communication, 1985).

• *Surface albedo.* Surface albedo is changed either by the addition of glacial ice on land or sea ice on ocean or by a change in bare land albedo. Surfaces that are covered with glacial ice (at 18 kyr BP and subsequently) are assigned an albedo of 0.80. The one exception is the North American ice sheet at 9 kyr BP, which is assigned an albedo of 0.50; we assume this is old ice, perhaps ponded with meltwater and dirty. Bare land albedo for 18 kyr BP is changed from the control case (0 kyr BP) values only if the CLIMAP-estimated albedo difference, 18 kyr BP minus modern, is greater

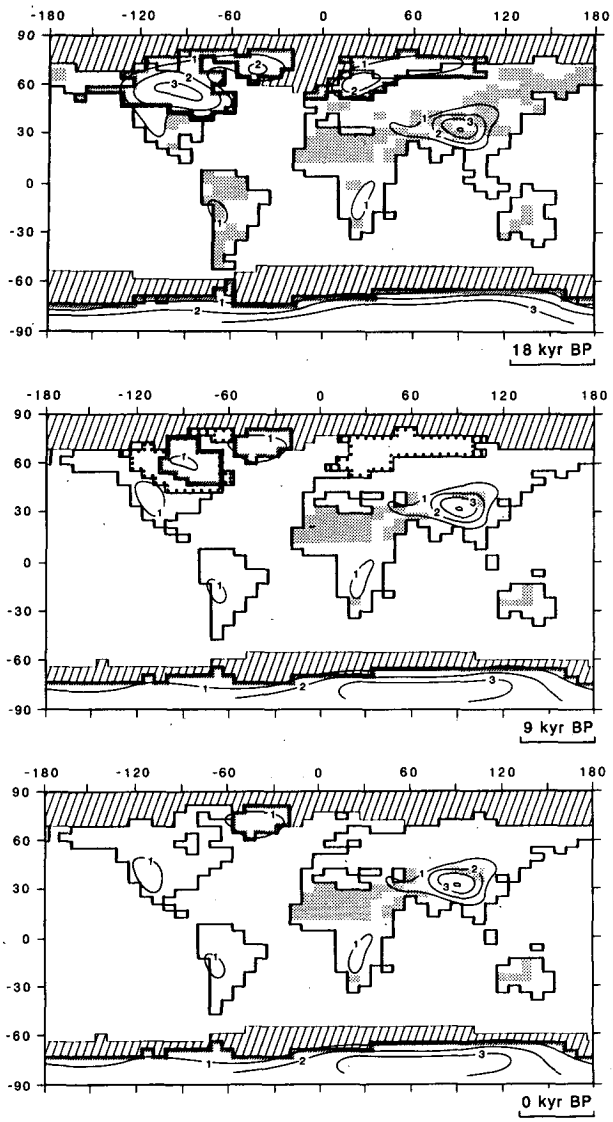

FIG. 2. Lower boundary conditions for 18 kyr BP (top), 9 kyr BP (middle), and the 0 kyr BP control (bottom): continental outlines, glacial ice (outlined with short hatch marks), July sea ice (diagonal stripes), topographic height (km), and bare land albedo. Topographic height is shown for both mountains and ice sheets. Land albedo is either 0.13 (clear) or 0.25 (stippled). Albedo of glacial ice is 0.80, except 0.50 for the North American ice sheet at 9 kyr BP. The 9 kyr BP map also shows the ice sheet boundaries for North America and Europe at 12 kyr BP (dotted border). January sea ice boundaries and January and July sea surface temperatures are shown in Figs. 5 and 10. Sea ice albedo is 0.70.

than one-half of the albedo difference between the two surface types in the control simulation: nondesert albedo, 0.13; and desert albedo, 0.25 (or, in some cases, between a land surface albedo and that of ice or snow, 0.80). Use of this rule kept the 18 kyr BP land albedo the same as the 0 kyr BP value at most locations. The two exceptions are parts of South America and central Asia—see Fig. 2. The albedos at 15 kyr BP and 18 kyr BP are identical. At 12 kyr BP, bare land albedos are set halfway between 18 kyr BP (15 kyr BP) and modern values in the two locations mentioned. At 9 kyr BP and thereafter, land albedos are the same as for 0 kyr BP.

Snow cover is prescribed in the model so that snow-albedo-temperature feedbacks are excluded (except insofar as they derive from the prescribed changes in glacial ice and sea ice). The land is snow-covered north of 68.9°N in July and of 42.2°N in January for all experiments; in the Southern Hemisphere, Antarctica is always snow covered.

4. Results

We present the simulation results in four levels of detail: a) global and hemispheric averages; b) zonal averages; c) global maps; and d) selected regional averages.

a. *Global and hemispheric averages*

1) *Radiation.* The increased seasonality of solar radiation in the Northern Hemisphere and decreased seasonality in the Southern Hemisphere reached extremes (compared to 0 kyr BP or 18 kyr BP) near 9 kyr BP (Fig. 3a). For the Northern Hemisphere, solar radiation was 37 W m^{-2} (8%) greater in July (summer) at 9 kyr BP than at 0 kyr BP (or 18 kyr BP). It was decreased by 18 W m^{-2} (−8%) in January at 9 kyr BP. For the Southern Hemisphere, January (summer) radiation was decreased by 28 W m^{-2} (−6%) at 9 kyr BP, whereas it was increased in July (11 W m^{-2}, 5%). However, the annual-average radiation change (global and hemispheric average) was near zero throughout the 18 000-year period.

2) *Temperature.* Global-average surface temperature (land plus ocean) was about 4 K lower than present at 18 kyr BP in both July and January and rose to near modern values by 9 kyr BP (Table 7). The temperature lowering for July 18 kyr BP was similar to the results obtained in previous AGCM experiments: Gates (1976b), 4.8 K; Manabe and Hahn (1977), 5.4 K. Hansen et al. (1984) found that annual-average temperature at 18 kyr BP was 3.6 K lower than at present.

Between 18 and 15 kyr BP, the July land-surface temperature increased by about 2 K in the Northern Hemisphere (Fig. 3b). Because the prescribed lower boundary conditions for 15 kyr BP and 18 kyr BP were identical, this warming was caused by the increased July insolation (Fig. 1, 3a). The general trend toward warmer conditions continued from 15 to about 9 kyr BP in both hemispheres, with the rise of both July and January temperature being the result of the adjustments of prescribed lower boundary conditions (land and sea ice extent, SST, land albedo) and the changed seasonality of temperature (i.e., July warming more than January in the Northern Hemisphere) (Fig. 3b) being the result of the changed seasonality of solar radiation (Fig. 3a).

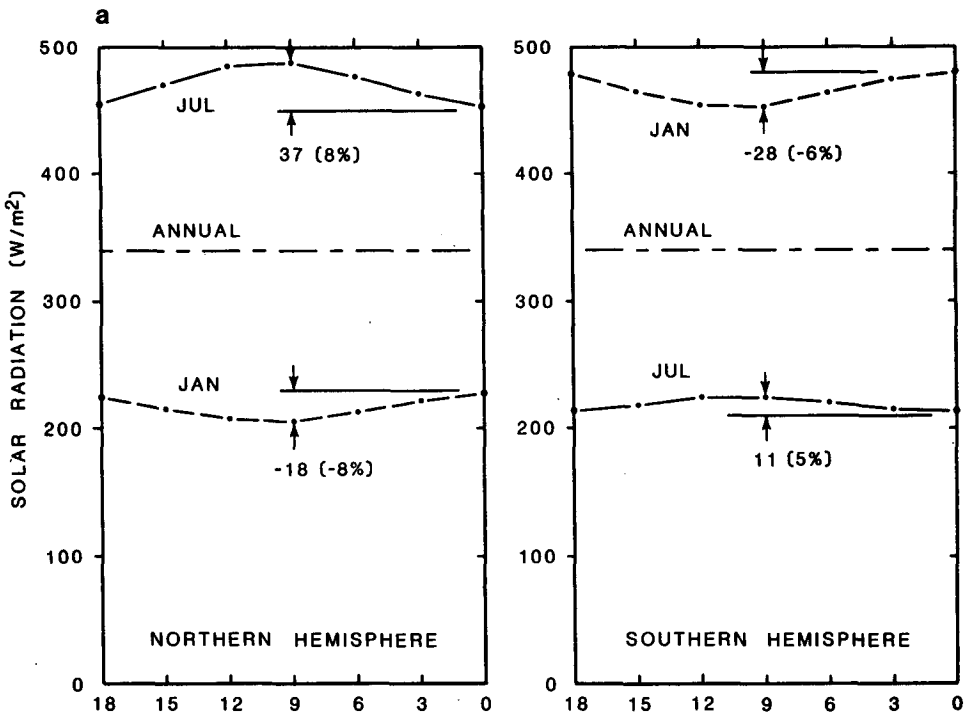

FIG. 3a. Solar radiation (W m^{-2}) for July, January, and annual-average for Northern and Southern hemispheres. Values are for 18 kyr BP to 0 kyr BP in 3000-year intervals.

The two hemispheres showed significant differences in the magnitude and timing of post-glacial warming. Land surface temperature increased by about 7 K in July from 18 to 9 kyr BP in the Northern Hemisphere (Fig. 3b). In the Southern Hemisphere, the January land surface temperature remained near glacial (18 kyr BP) levels until about 9 kyr BP and only then began rising toward the 0 kyr BP value (Fig. 3c). This delayed warming occurred because the trend toward cooler summers produced by the orbital changes counteracted the prescribed adjustment (between 15 and 9 kyr BP) of lower boundary conditions toward modern values (Fig. 1). Thus, the warming of the land surface in the "growing season" was much delayed in the Southern Hemisphere (occurring largely between 9 and 0 kyr BP) compared to the Northern Hemisphere (occurring largely between 18 and 9 kyr BP). It was also of smaller magnitude (2 K versus 7 K, respectively) owing to the smaller land area, the absence of additional glacial-age ice, and the somewhat smaller radiation changes.

At 9 and 6 kyr BP, when seasonality of the Northern Hemisphere climate was greater than at present, the northern land surface was about 1 K warmer in July and about 0.5 K colder in January than now (Fig. 3b; Table 7). At the same time, seasonality of temperature in the Southern Hemisphere was reduced because perihelion was in southern winter at 9 kyr BP, but in southern summer now; thus, it was about 2 K colder in January (summer) and about 1 K warmer in July (winter) (Fig. 3c).

The estimated annual-average temperature was close to the modern value at 9 kyr BP and thereafter because the changes of seasonal extremes (warmer July, colder January, or the opposite) largely cancelled in the weighted estimate of annual-average temperature (Table 7).

3) *Sea level pressure.* In response to changes in the seasonal cycle of solar radiation, there were adjustments in the distribution of atmospheric mass between land and ocean as the temperature of the land changed relative to the ocean. Thus, with the increased warmth over the Northern Hemisphere continents centered around 12 to 6 kyr BP in July, sea level pressure was lower over land (by about 2 mb) and higher over ocean (by about 0.25 mb) (Fig. 3b). Conversely, the sea level pressure was higher over southern land in southern summer (Fig. 3c). The increased (decreased) pressure gradient force from ocean to land was associated with stronger (weaker) northern (southern) summer monsoons between 12 and 6 kyr BP.

In January, 18–15 kyr BP, sea level pressure was higher over northern continents (and lower over the northern oceans) because of the much lower land temperature associated with the large continental ice sheets. (The calculated global-average sea level pressure increased from the control-case values for the experiments with glacial ice. In order to make comparisons with the control simulation, we subtracted this global-average bias from the results; see also Gates, 1976b.)

4) *Hydrologic budget.* Large changes in the hydro-

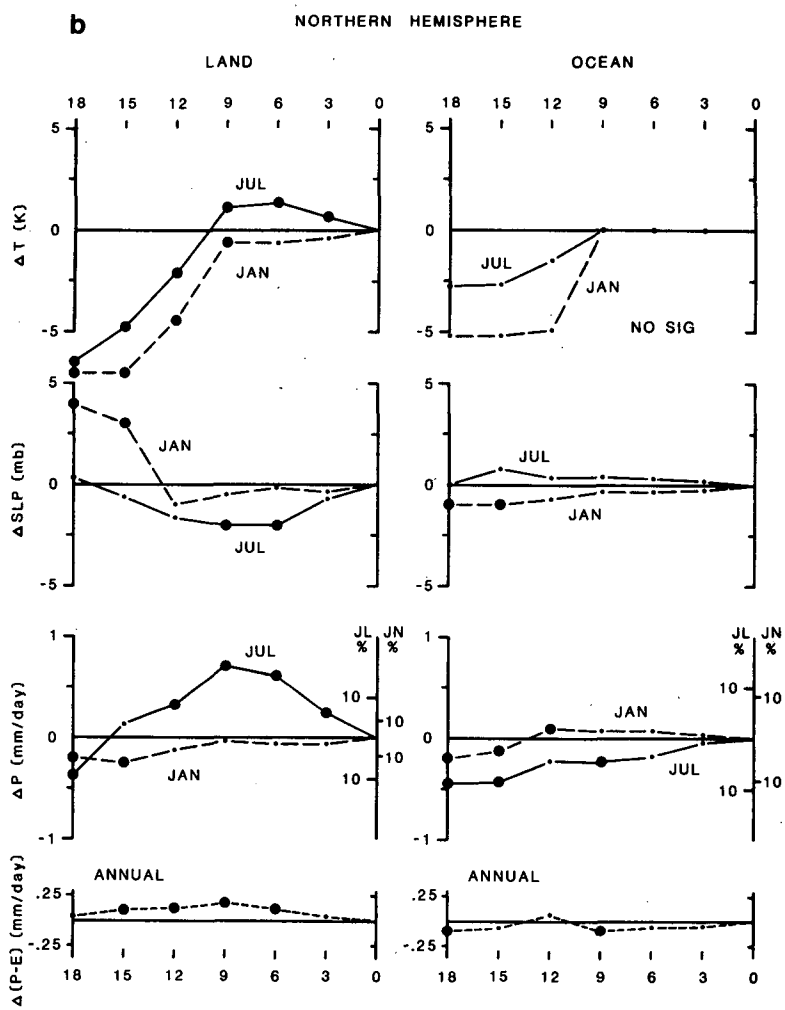

FIG. 3b. Surface temperature departures (ΔT, K), sea level pressure departures (ΔSLP, mb), precipitation departures (ΔP, mm day^{-1}) and precipitation-minus-evaporation departures [$\Delta(P-E)$, mm day^{-1}] for July and January, for Northern Hemisphere land and ocean, and for the period 18 kyr BP to 0 kyr BP in 3000-year intervals. The values for ocean include both open ocean and sea ice grid points. Departures are expressed as the paleoclimatic experiment minus the control (0 kyr BP) experiment. A large dot indicates that the departure is statistically significant (two-sided t test) at or above the 95% confidence level based upon the model's natural variability. Ocean surface temperature is prescribed and therefore no measure of statistical significance is computed for it. For precipitation, the ordinate on the right indicates plus and minus 10% departures for July (JL) and January (JN).

logic cycle were caused by the glacial-age boundary conditions and the variations in orbital parameters. Global-average precipitation and evaporation were 7% lower in July 18 kyr BP, and 3% lower in January 18 kyr BP than at present (Table 7). This result for July 18 kyr BP was similar to, but less than, the precipitation reduction obtained in previous AGCM experiments: Gates (1976b), a 14% reduction; Manabe and Hahn (1977), a 10% reduction. We used estimates of sea surface temperature for 18 kyr BP (CLIMAP, 1981) that are not as low as earlier estimates (CLIMAP, 1976). This difference in boundary conditions may explain, in part, the smaller reduction in the intensity of the hydrologic cycle found in this study.

Beginning at 15 kyr BP and culminating between 12 and 6 kyr BP, precipitation increased over Northern Hemisphere land in northern summer and decreased over Southern Hemisphere land in southern summer (Figs. 3b, c); compared to present, these changes at 12–6 kyr BP were of order 10–20% and were highly significant statistically. The precipitation departures over the ocean were generally of opposite sign to the changes over land so that global-average precipitation and evaporation remained close to present values; for ex-

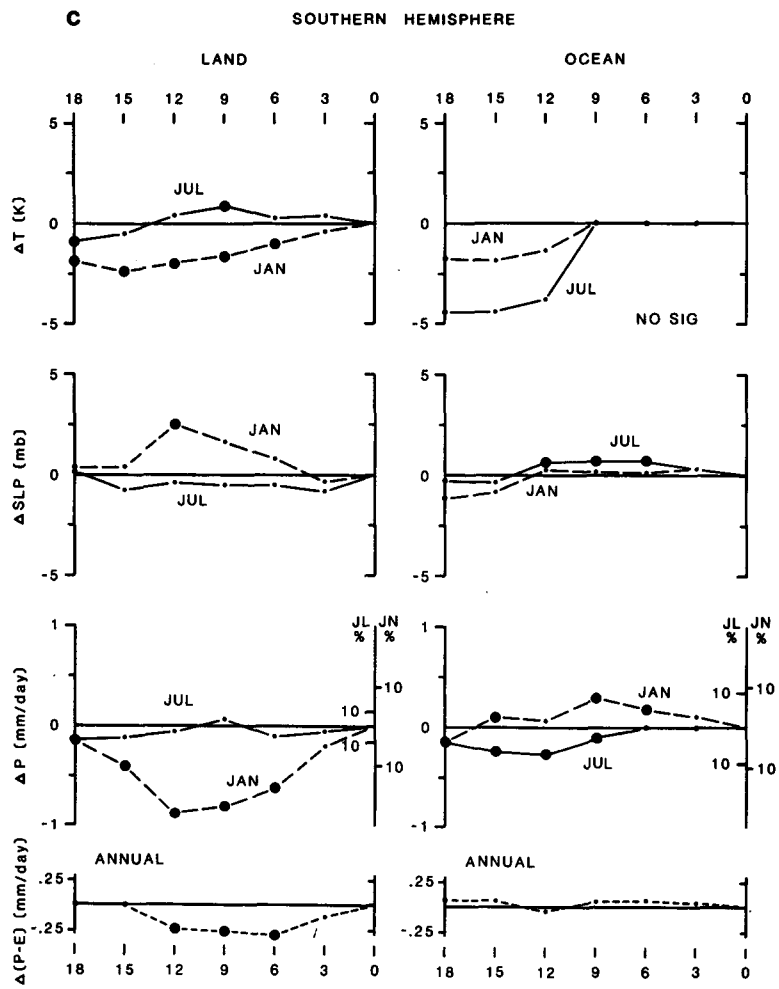

FIG. 3c. As in 3b except for the Southern Hemisphere.

ample at 9 kyr BP they were 2% higher in both July and January than at present. The changes in summer precipitation were consistent with the sea level pressure changes; for example, at 9 kyr BP the sea level pressure over northern land was lower in July (strengthened monsoon lows with increased precipitation) and the oceanic high pressure cells were strengthened (with decreased precipitation).

Changes in precipitation minus evaporation ($P - E$) over land (annual average estimate) were generally of the same sign as the changes in precipitation, but of smaller magnitude. $P - E$ was increased over northern continents (15 to 6 kyr BP) and decreased over southern continents (12 to 6 kyr BP). Changes in $P - E$ over the oceans were generally of opposite sign to changes over land, but were statistically significant only at 18 and 9 kyr BP for the northern oceans (Figs. 3b, c).

b. *Zonal averages*

In this section, we use latitude–time plots to portray the zonal-average changes of five climatic variables (temperature, sea level pressure, vertical motion, zonal wind and the hydrologic budget) to the zonally symmetric changes of solar radiation and the changes of glacial-age boundary conditions. The glacial-age boundary condition changes are, of course, not zonally symmetric (for example, in the case of the North American–West European ice sheets and the southward-extended North Atlantic sea ice) but nevertheless have a significant zonal-average component (CLIMAP Project Members, 1981; see also Figs. 5 and 10).

1) *Radiation.* The zonal distribution of solar radiation changes, 18 to 0 kyr BP (Fig. 4a) shows the combined effects of changes of date of perihelion, eccentricity, and axial tilt. For 9 kyr BP, when perihelion occurred in July and the axial tilt was at a maximum, the largest increases of radiation in July were in high northern latitudes; moreover, the increases were larger in the northern tropics than in the southern tropics. In southern high latitudes in January (summer), the increased tilt at 9 kyr BP worked to moderate the seasonal changes associated with the perihelion change. Thus,

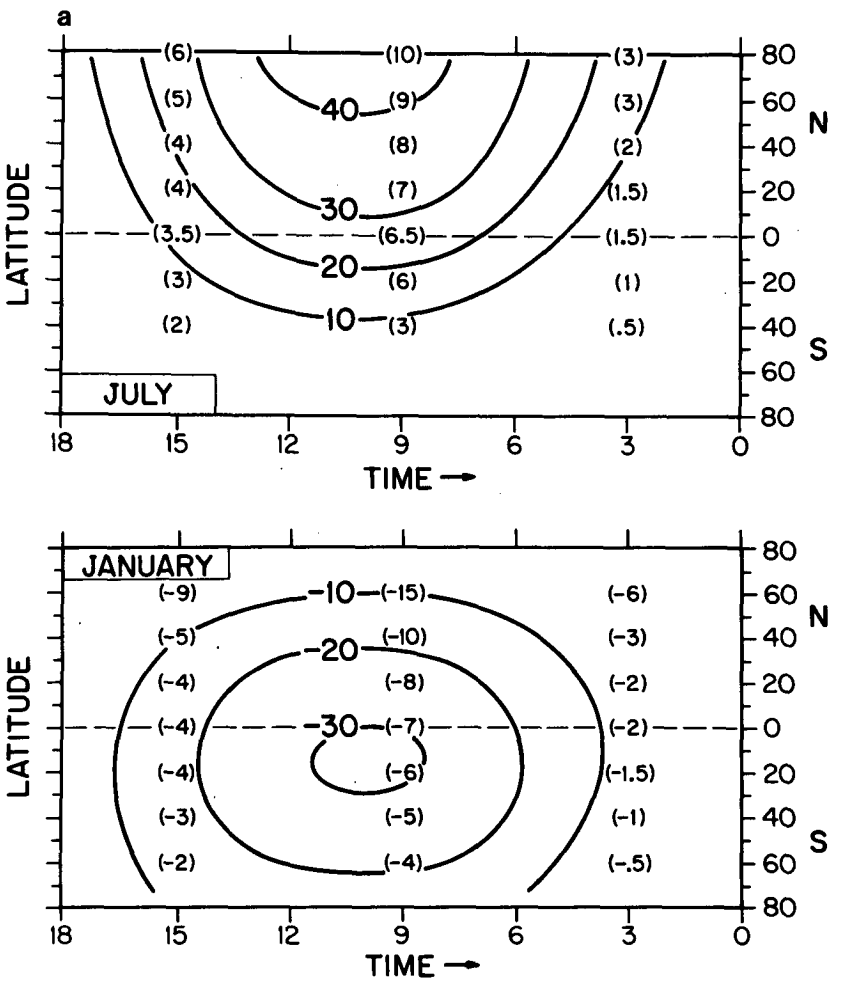

FIG. 4a. Solar radiation departures (past-minus-present, in W m^{-2}) for July and January as a function of latitude and time (18 kyr BP to 0 kyr BP). The numbers in parentheses are the departures from present expressed in percent.

the largest decrease of radiation in January was in the southern tropics rather than southern high latitudes.

2) *Temperature and sea level pressure.* Figures 4b, c show large changes in the zonal-average temperature and pressure distribution from 18 kyr BP to present. In July, at 18 and 15 kyr BP, the land surface temperature was much colder than present (by 5–15 K) in the latitudes occupied by glacial ice, 45–70°N, and sea level pressure was increased in the same latitudes. The temperature was about 2 K lower throughout the tropics. At 15 kyr BP the northern land temperature began to increase and it approached modern levels at 12 kyr BP, except at the latitudes of the ice sheets. By 9 kyr BP, the land was 1–2 K warmer than at 0 kyr BP from 85°N to 30°S, except for the narrow band at 50–70°N where part of North America remained ice covered (Fig. 2). Warming was greatest and reached greatest statistical significance in the latitude band 15–50°N at 9 and 6 kyr BP. The sea level pressure over land was lower in the same latitudes starting at 15 kyr BP and culminating between 12 and 6 kyr BP. The maximum lowering of pressure over land was about 3 mb at 20–35°N.

In January, the cooling at 18–12 kyr BP was a maximum in northern subpolar and midlatitudes, but it reached 4 K in the northern and 2–3 K in the southern tropics as well. After 12 kyr BP, the January temperature was close to the 0 kyr BP value in northern midlatitudes and well within the range of the model's natural variability, but cooler conditions persisted in the tropics until after 6 kyr BP. The latitudinal distribution of the temperature departures during the period 15 to 6 kyr BP (Fig. 4b) was consistent with the insolation departures (Fig. 4a); the insolation changes (compared to present) were small in high northern latitudes and largest in the tropics.

The sea level pressure over land was highest at 18–15 kyr BP in mid- to high northern latitudes (associated with glacial anticyclones). In both northern and southern tropical lands, the January sea level pressure de-

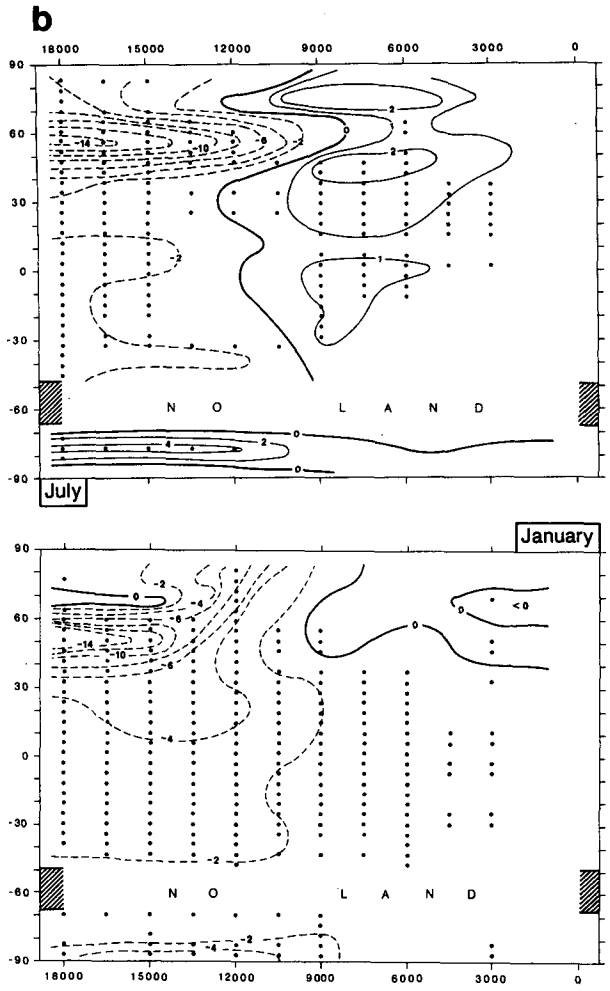

FIG. 4b. Temperature departures (K) for the land surface for July (top) and January (bottom) as a function of latitude and time (years before present). Dots indicate that the departure is statistically significant (two-sided t test) at or above the 90% confidence level based upon the model's natural variability. Values for experiments were linearly interpolated to the midpoints between the experiments (16.5, 13.5, 10.5, 7.5, 4.5, 1.5 kyr BP) for continuity of analysis.

partures were positive from about 15 to 6 kyr BP, during the period of low temperatures and reduced insolation. In the Southern Hemisphere lands, the higher sea level pressure was associated with weakened summer monsoons. The lower January sea level pressure over Northern Hemisphere lands in mid- and high latitudes at 12 and 9 kyr BP was related in part to the reduced height and size of the ice sheets (compared to 15 kyr BP); a large area of low surface pressure developed downstream from the North American ice sheet and extended into Western Europe at 12 kyr BP (not shown). After 12 kyr BP, the small positive temperature departures and the negative sea level pressure departures at high latitude northern lands were related to advective processes caused by the reduced insolation (see section 4c, below); however, these changes were generally within the range of the model's natural variability.

3) *Vertical motion.* Changes in north–south and east–west vertical circulation cells were prominent features of the experiments (Fig. 4d). At 18 kyr BP in July upward vertical motion over northern tropical land and downward motion over southern tropical land were strengthened, compared to present. This change from present was part of a slight overall increase in the intensity of the dominant (zonal-average) southern Hadley cell that straddles the equator in July (not shown). Whereas Manabe and Hahn (1977) also report an increased intensity of the southern Hadley cell for July 18 kyr BP, their simulation showed that the increase resulted primarily from changes over ocean and that the changes over land were of opposite sign (unlike our results). The upward motion over northern tropical lands strengthened further and shifted northward beginning at 15 kyr BP, and remained stronger and fur-

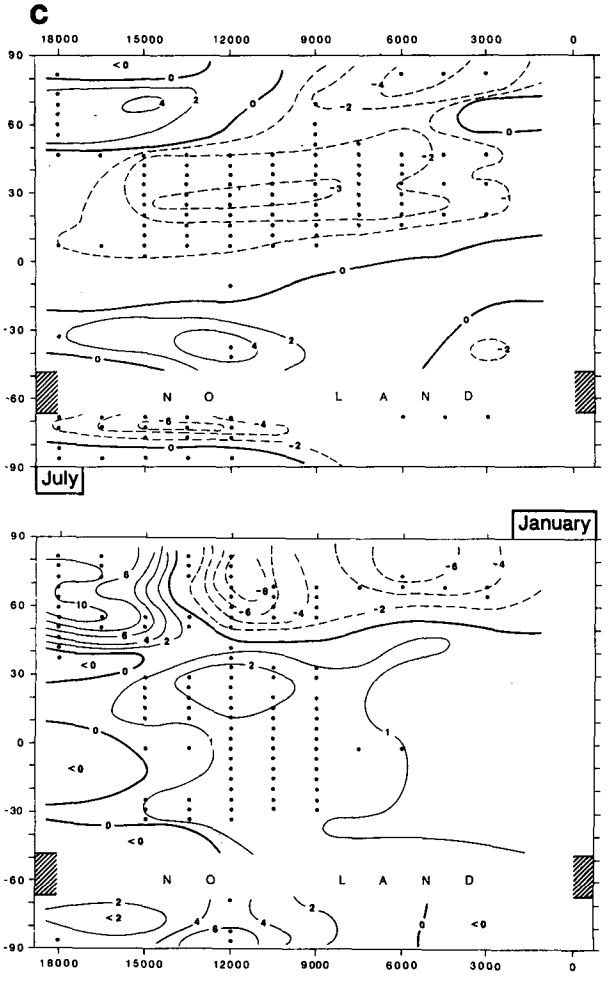

FIG. 4c. Sea level pressure departures (mb) for the land surface for July (top) and January (bottom) as a function of latitude and time (years before present). See caption 4b for further details.

ther north than at present until after 6 kyr BP; the position of the vertical motion contour labeled −2 illustrates these changes (Fig. 4d). Moreover, the narrow band of downward motion at about 30°N (18–15 kyr BP and 3–0 kyr BP) disappeared at 12 to 6 kyr BP and upward motion was strengthened as far north as 40°N.

In January, the upward vertical motion over Southern Hemisphere land was weakest in the interval 12 to 6 kyr BP. The upward motion at that time was less than half its value at 18–15 and 3–0 kyr BP. Downward vertical motion over northern tropical lands and upward vertical motion over southern tropical lands were strengthened slightly at 18 and 15 kyr BP. This change was part of a slight overall increase in the intensity of the dominant (zonal-average) northern Hadley cell that straddles the equator in January (not shown).

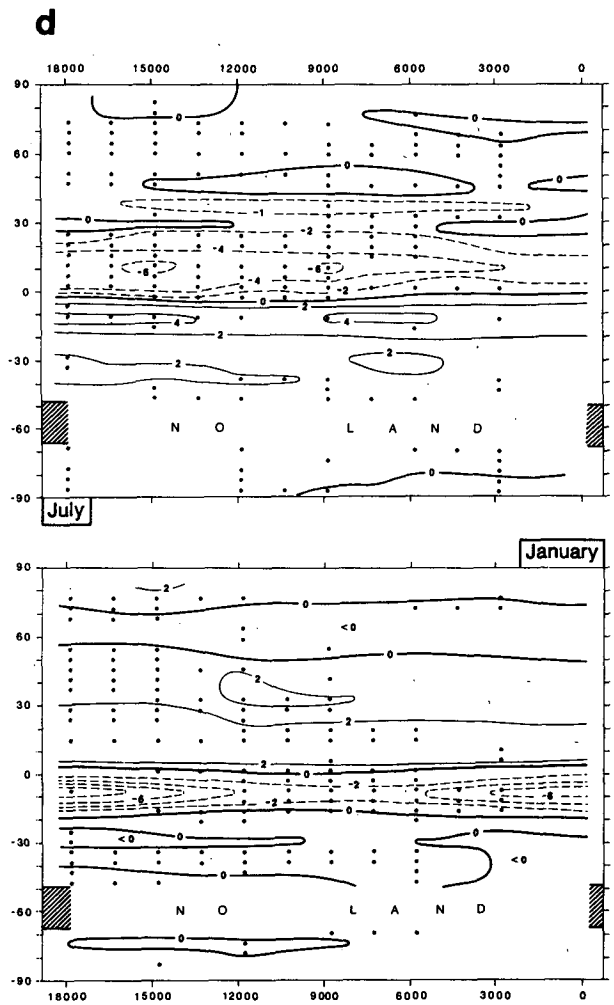

FIG. 4d. Vertical motion (10^{-4} mb s^{-1}) at sigma level 0.5 (approximately 500 mb or 5.5 km) over the land surface for July (top) and January (bottom) as a function of latitude and time (years before present). Negative values indicate upward motion. Multiplying the values by −5 gives approximate vertical motion in meters per hour. See caption 4b for further details.

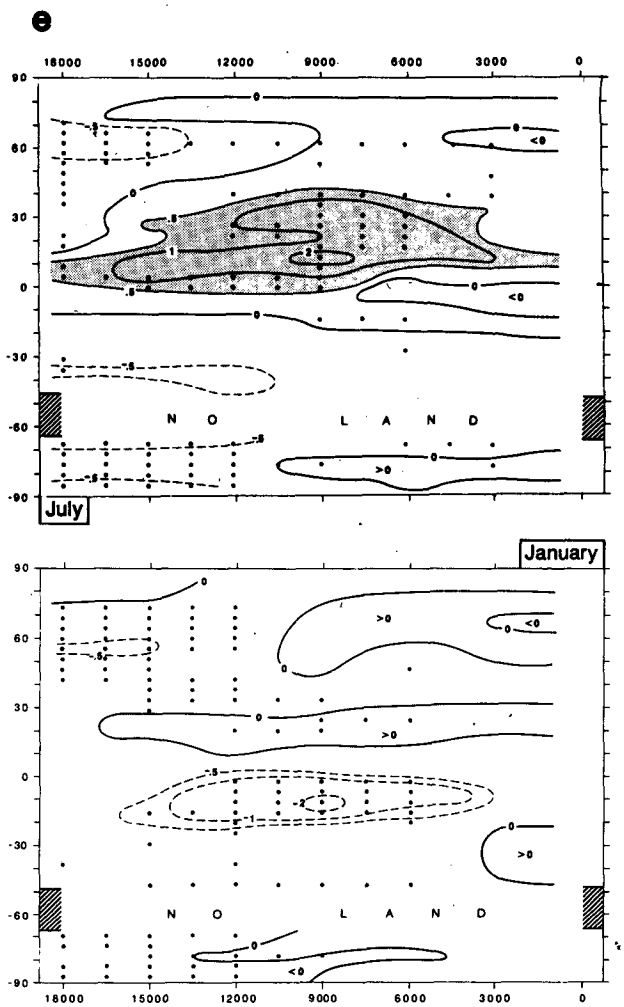

FIG. 4e. Precipitation departures (mm day^{-1}) for the land surface for July (top) and January (bottom) as a function of latitude and time (years before present). Precipitation fields were smoothed using a two-dimensional, nine-point, binomial filter. See caption 4b for further details.

For the period 12 to 6 kyr BP, changes in vertical motion over the oceans were generally opposite to those over land at the same latitude. This inverse relationship indicates that east–west circulation cells were an important feature of the model's response to orbital forcing. The zonal-average Hadley circulation at 9 kyr BP (both July and January) was of approximately the same strength and orientation as at 0 kyr BP (not shown).

4) *Hydrologic budget.* Figure 4e shows major shifts in the zonal distribution of precipitation from 18 kyr BP to present. Precipitation was decreased at most latitudes for the period 18 to 12 kyr BP for both January and July, but especially in the latitudes of the ice sheets (45–70°N). Precipitation increased in the latitude band 0–30°N by 15 kyr BP and remained higher than present through the period 12 to 6 kyr BP (see also Fig. 15). In the Southern Hemisphere, precipitation over land

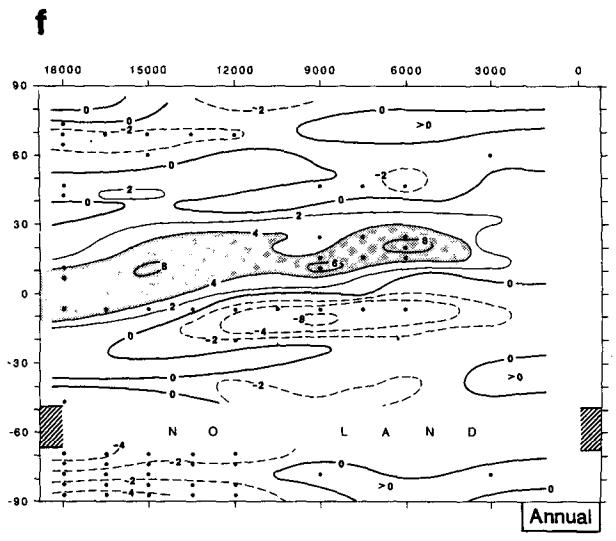

FIG. 4f. Precipitation-minus-evaporation departures (10^{-1} mm day^{-1}) for the land surface for estimated annual conditions as a function of latitude and time (years before present). See text for method of estimating the annual average. Precipitation and evaporation fields were smoothed using a two-dimensional, nine-point, binomial filter. See caption 4b for further details.

was significantly decreased from 0–15°S in January, 12 to 6 kyr BP.

Figure 4f shows the zonal distribution of $P - E$ departures (estimated annual-average) for the land surface. With the generally cooler conditions over the glacial ice at 18 to 9 kyr BP, evaporation decreased even more than precipitation so that, especially at 45–55°N, $P - E$ increased slightly compared to present. At 6 kyr BP, this same latitude band had decreased $P - E$, compared to present, because the precipitation increased less than the evaporation. In the tropical lands, $P - E$ was slightly larger at 18 kyr BP than at 0 kyr BP because evaporation decreased more than precipitation. With the strengthened northern summer monsoons and weakened southern summer monsoons from 12 to 6 kyr BP, $P - E$ was increased in the zone 0–30°N and decreased in the zone 0–20°S.

5) *Zonal-average winds.* The mid-to-upper-tropospheric zonal wind distribution reflects features of the surface temperature distribution, consistent with the thermal wind relationship (Fig. 4g). In July 18–15 kyr BP, the strongest westerlies were at 45°N, along the southern edge of the ice sheets where the horizontal north–south temperature gradient was large. A local minimum in the westerlies occurred at around 60°N—the latitude of maximum westerlies at 0 kyr BP;—and a weak secondary maximum occurred around 70°N, along the northern flank of the ice sheets. The southern July (winter) westerlies were about 5 m s^{-1} stronger than present from 18 to 12 kyr BP in the region of the northward-extended sea-ice border (about 50°S), and the zonal wind maximum was shifted about 10°–15° of latitude south of its present position. Equatorial easterlies were also strengthened at glacial maximum. Similar changes of the northern westerlies and equatorial easterlies occurred in the August 18 kyr BP simulation by Gates (1976b), but not the large shift of the southern westerlies. Between 12 and 9 kyr BP the zonal wind distribution adjusted to near present conditions, except that the equatorial easterlies remained strong until after 9 kyr BP.

Zonal winds at 500 mb in January (Fig. 4g) were more than 5 m s^{-1} stronger at 18–15 kyr BP than at 0 kyr BP in the band 30–45°N, along the southern edge of the northern hemisphere ice sheets; winds were about 5 m s^{-1} weaker over the ice sheet (50–65°N). At 12 kyr BP, with the ice sheet reduced in height and area, the zonal flow weakened along the southern flank of

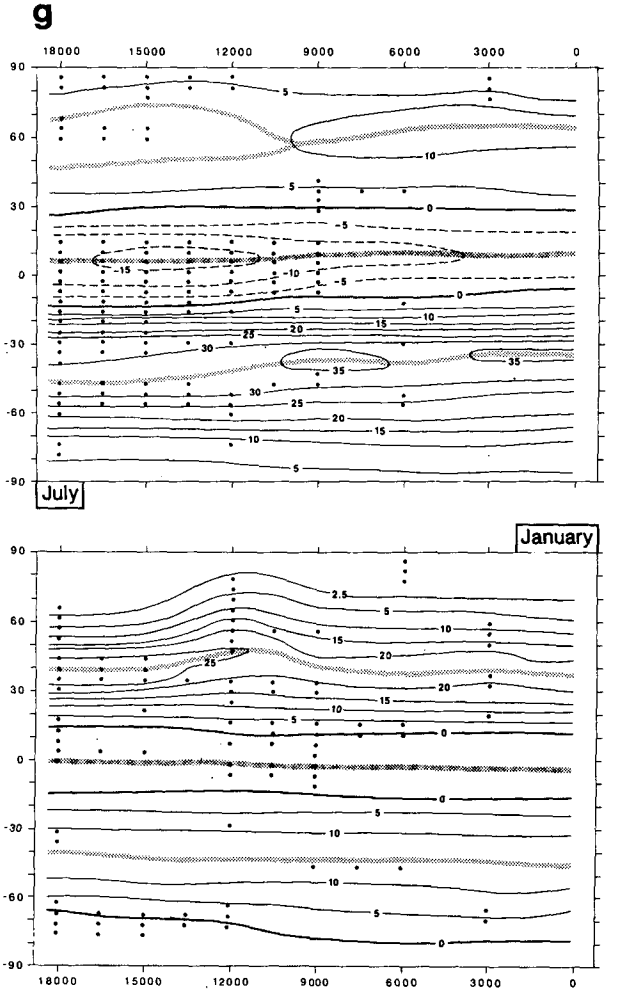

FIG. 4g. Zonal average u-component wind (m s^{-1}) at sigma level 0.189 (about 190 mb or about 12.2 km) for July (top) and at sigma level 0.5 (about 500 mb or about 5.5 km) for January (bottom) as a function of latitude and time (years before present). Negative values (dashed) denote easterlies. Shaded band indicates latitude of relative maxima. See caption 4b for further details.

the ice sheets and strengthened farther north, as the maximum flow developed over the glacial ice rather than being split to the north and south.

Zonal-average surface winds (sigma = 0.991; about 100 m), not shown, exhibited some of the same features as the mid-to-upper troposphere winds. North of 70°N the zonal-average flow was westerly from 18 to 12 kyr BP, due to the establishment of westerly flow along the northern flanks of the North American and European ice sheets.

In the tropics, changes in zonal-average u-component winds were small throughout most of the period 18 to 0 kyr BP. At 18–15 kyr BP the northern equatorial easterlies were slightly stronger (by about 10%) and the southern equatorial easterlies were slightly weaker than present; however, the differences were of marginal statistical significance. At 9 kyr BP in July, the northern tropical easterlies were weakened (primarily because of stronger westerlies over land) and the southern tropical easterlies were strengthened.

c. *Global maps of climate for 18, 9 and 0 kyr BP*

Many features of the simulated climates have significant zonally-asymmetric, land-ocean components that can be illustrated best with selected global charts. In this section, we show charts for 18, 9 and 0 kyr BP, and for the 18 kyr BP-minus-0 kyr BP and 9 kyr BP-minus-0 kyr BP differences to illustrate these regional features. In general, we first discuss the simulated changes in surface temperature and then the changes in sea level pressure, winds aloft and at the surface, storm tracks, and the hydrologic cycle.

1) *18 kyr BP—July.* The prescribed changes of land ice, sea ice, and ocean surface temperature produced major changes in glacial-age regional climates. Surface temperature was lower on all continents, and much lower in the vicinity of the Northern Hemisphere ice sheets (by 20–30 K) and over the equatorward-extended sea ice of both hemispheres (by 10–15 K); even over

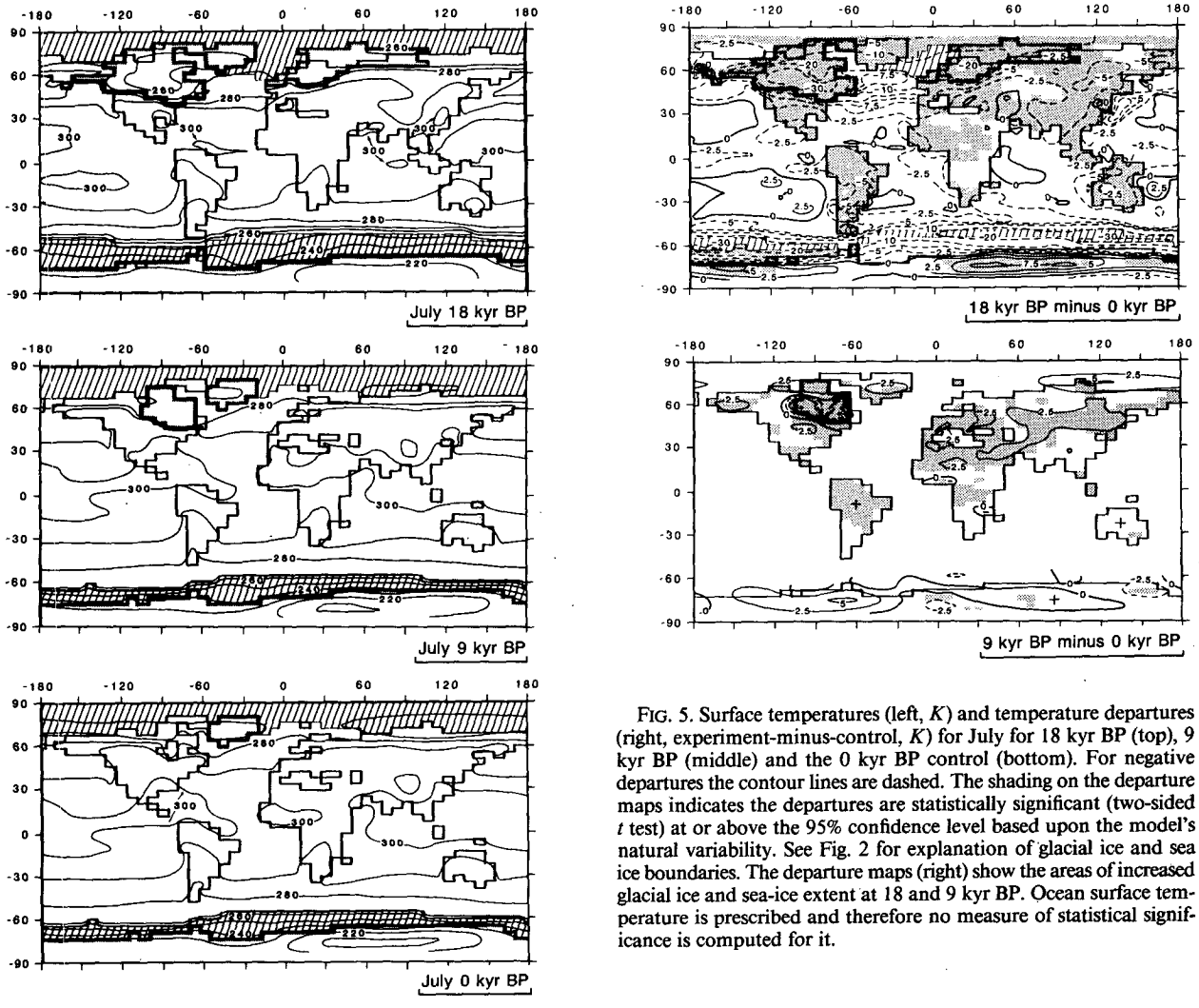

FIG. 5. Surface temperatures (left, K) and temperature departures (right, experiment-minus-control, K) for July for 18 kyr BP (top), 9 kyr BP (middle) and the 0 kyr BP control (bottom). For negative departures the contour lines are dashed. The shading on the departure maps indicates the departures are statistically significant (two-sided t test) at or above the 95% confidence level based upon the model's natural variability. See Fig. 2 for explanation of glacial ice and sea ice boundaries. The departure maps (right) show the areas of increased glacial ice and sea-ice extent at 18 and 9 kyr BP. Ocean surface temperature is prescribed and therefore no measure of statistical significance is computed for it.

tropical lands the temperature was 2–4 K lower (Fig. 5). Sea level pressure was increased in the vicinity of the northern ice sheets/sea ice and decreased south of the ice sheet/sea ice margin (Fig. 6).

The core of the North Atlantic westerly jet was centered above the southern margin of the North Atlantic sea ice (Fig. 7) and was about 5–10 m s^{-1} stronger than at 0 kyr BP. Westerly winds were also stronger on the southern flank of the North American ice sheet. The westerly flow split around the North American ice sheet, with the strongest winds along the southern flank, weak winds over the ice sheet, and a secondary maximum along the northern flank. The Southern Hemisphere westerlies were shifted south over the northward-extended sea ice limit; this increased wind speeds by about 10 m s^{-1} around 50°S and decreased winds by a comparable amount around 30°S. The high-level easterlies over North Africa and the tropical Atlantic were also strengthened by 10 m s^{-1} or more (Fig. 7; Fig. 4g). Northern Hemisphere storm tracks were shifted far south and were situated along the southern edge of the North American and European ice sheets and the North Atlantic sea ice margin; the higher values of standard deviation in the southern ocean suggest more intense or more frequent storms, or both (Fig. 8).

Precipitation (Fig. 9) was generally lower than at 0 kyr BP across North America, the North Atlantic, Europe, and where sea surface temperature was lower at 18 kyr BP than at 0 kyr BP (e.g., the western equatorial Pacific, the western North Pacific, and most of the Atlantic and Indian oceans). Increased precipitation occurred over tropical East Africa, and over oceanic regions where the sea surface temperature was higher at 18 kyr BP than at 0 kyr BP (e.g., the subtropical North and South Pacific, the region just east of Australia, and the western equatorial Indian ocean).

2) *18 kyr BP—January.* The prescribed major

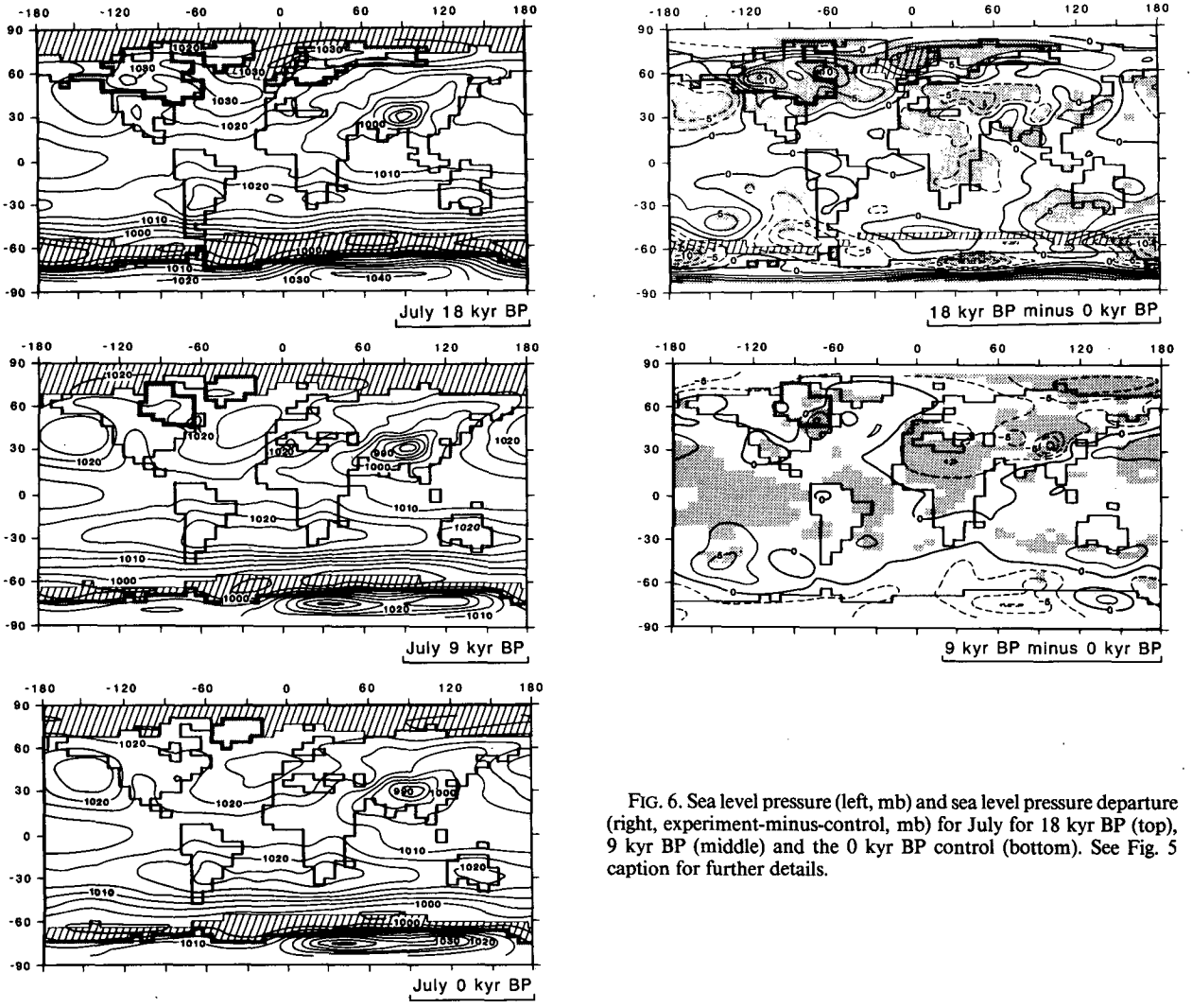

FIG. 6. Sea level pressure (left, mb) and sea level pressure departure (right, experiment-minus-control, mb) for July for 18 kyr BP (top), 9 kyr BP (middle) and the 0 kyr BP control (bottom). See Fig. 5 caption for further details.

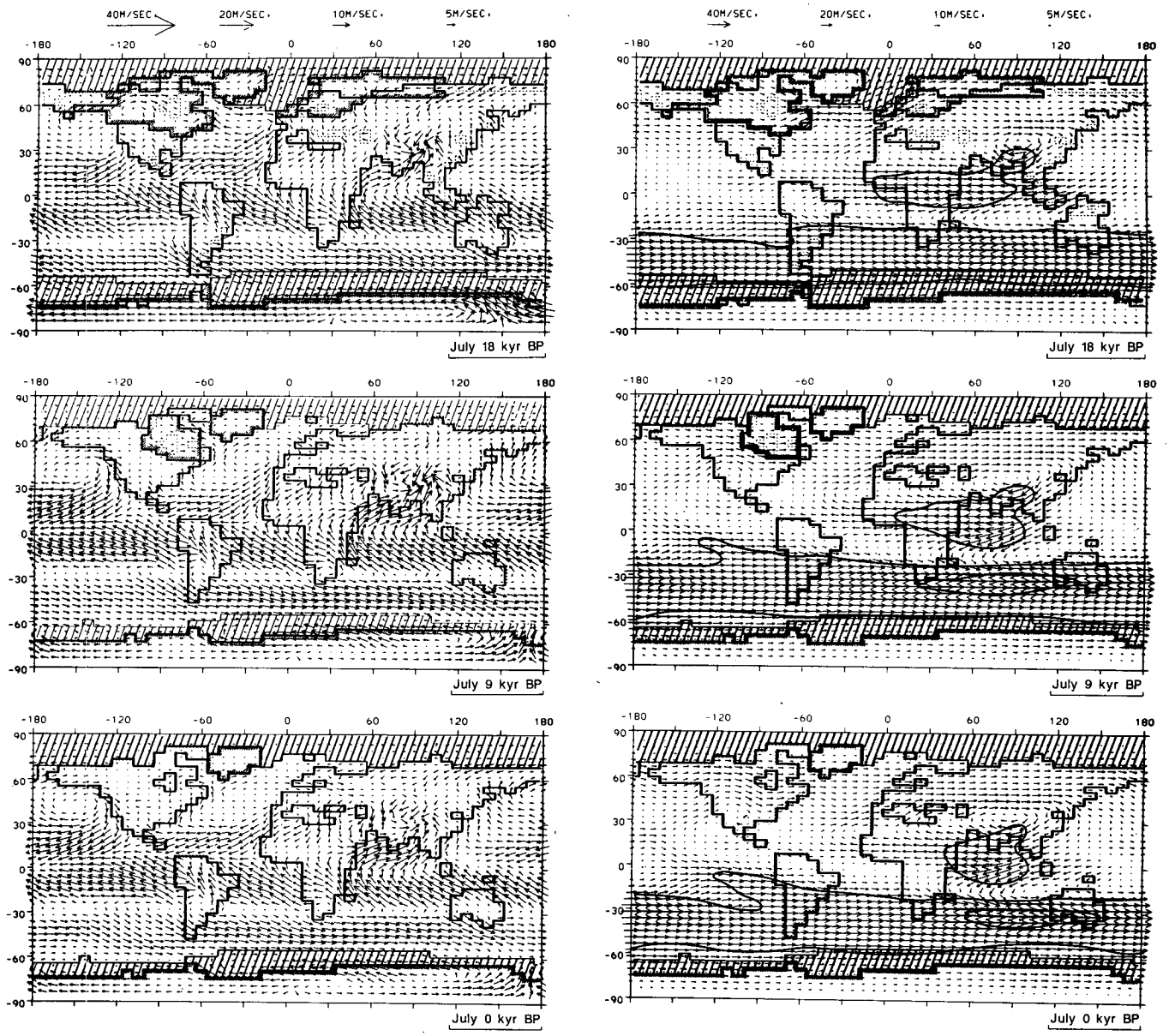

FIG. 7. Surface winds (left) and winds at sigma level 0.189 (about 190 mb or 12.2 km) (right) for July for 18 kyr BP (top), 9 kyr BP (middle) and the 0 kyr BP control (bottom). Arrows denote direction and magnitude (key at top of figures). For winds aloft, the 20 m s^{-1} and 40 m s^{-1} isotachs are shown.

equatorward extension of sea ice in the North Atlantic to about 45°N was of particular importance for the simulated January climate. The replacement of open ocean by sea ice over this large area of the North Atlantic decreased the surface temperature by 30–40 K (it is 10–15°C at 0 kyr BP and was −25 to −20°C at 18 kyr BP; Fig. 10). This temperature lowering increased the baroclinicity at the sea ice boundary and strengthened the equatorward-displaced North Atlantic jet. (The maximum speed was 40 m s^{-1} at 18 kyr BP, compared to 30 m s^{-1} at 0 kyr BP; Fig. 12.)

Another feature of major importance was the split in the westerly flow produced by the presence of the North American ice sheet. The southern branch developed over the eastern subtropical North Pacific and the southern United States. The northern branch brought southerly flow across Alaska and westerly flow along the northern flank of the ice sheet, and accounted for the advective warming of these regions at 18 kyr BP (Fig. 10). The northern branch recurved southward between the eastern flank of the North American ice sheet and Greenland and rejoined the southern branch of westerlies over the North Atlantic. Because of the split flow, the minimum zonal wind at 18 kyr BP (over the ice sheet) was at the latitude of the maximum zonal wind at 0 kyr BP (Fig. 12). A similarly split flow pattern

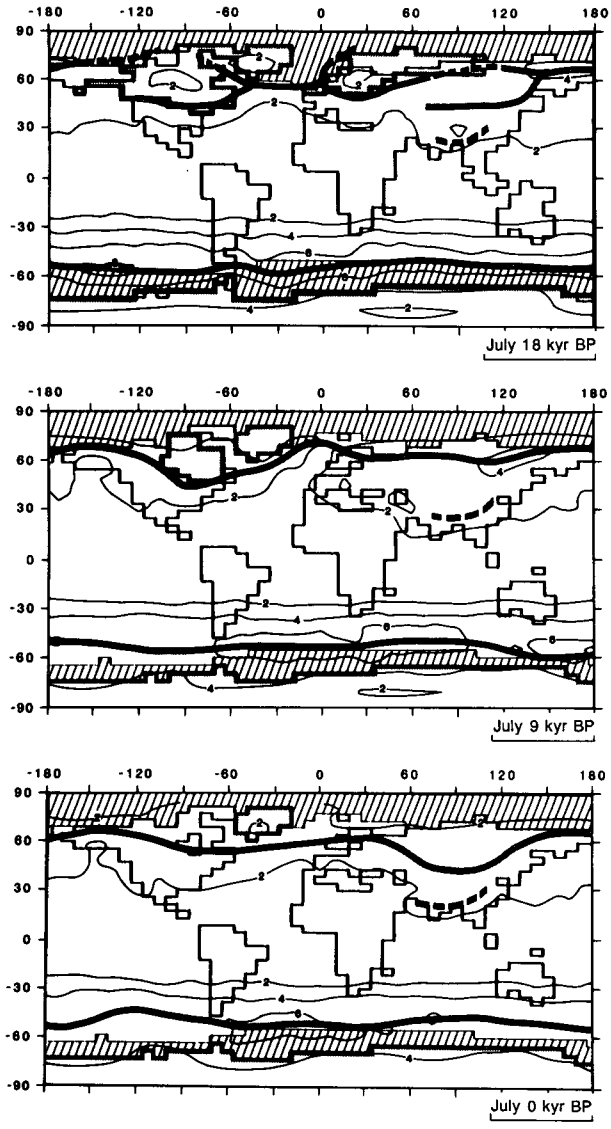

FIG. 8. Standard deviation of surface pressure (mb) for July for 18 kyr BP (top), 9 kyr BP (middle) and the 0 kyr BP control (bottom). The standard deviation is computed from the variance contained between periods of 2.5 and 6 days, using the band-pass filter described by Blackmon and Lau (1980). The shaded bands indicate the latitude of maxima; if broken, the maxima are less pronounced.

was simulated for 18 kyr BP with the general circulation model of the Geophysical Fluid Dynamics Laboratory (Manabe and Broccoli, 1985).

At the surface, glacial anticyclones formed over the North American and European ice sheets (Fig. 11, Fig. 12). These anticyclones were also present in July of 18 kyr BP (Fig. 7), but were less pronounced. Low-level outflow of cold air through the broad ice-valley between North America and Greenland (wind speeds up to 15 m s^{-1}) and east of Greenland (10 m s^{-1}) could have helped to develop and maintain the extensive sea ice cover (see Manabe and Broccoli, 1985).

On the northern flanks of the ice sheets, strong surface westerlies (5–10 m s^{-1}) occurred at 18 kyr BP where winds are weak or easterly at 0 kyr BP; as a result, the zonal-average winds along the Arctic coast north of 70°N were westerly at 18 kyr BP whereas they are easterly at 0 kyr BP. South of the North American ice sheet, surface easterlies or weak westerlies occurred where winds are strong westerly at 0 kyr BP. This helped to produce more "continental" conditions at 18 kyr BP with surface temperature lowered by 5–15 K (Fig. 10) and precipitation reduced (Fig. 14).

The vertical structure of the wind and temperature fields along a north–south cross section over the North American ice sheet at 90°W (not shown) shows, on the southern flank, weak surface easterlies giving way to strong westerlies at 500 mb (20 m s^{-1}). This vertical shear is supported in the temperature field by the very cold conditions over the ice sheet. Along the northern flank, with colder air to the south, strong surface westerlies (10 m s^{-1}) give way to weaker westerlies at 500 mb (5 m s^{-1}).

The major eastern Pacific-North American wintertime storm track (Fig. 13) was shifted about 20° of latitude south of its 0 kyr BP position, roughly paralleling the southern branch of the jet (Fig. 12) and the band of lowered sea level pressure (Fig. 11). Precipitation was increased in the central and eastern North Pacific (where CLIMAP-estimated SSTs were relatively warm at 18 kyr BP), across the southwest and southern United States, and along the North Atlantic sea ice border. This band of increased precipitation roughly paralleled the 18 kyr BP storm track and jet stream axis; however, the precipitation increases at individual gridpoints were generally not statistically significant.

In Europe, the strong westerly flow over the sea ice covered North Atlantic continued as westerlies strengthened across southern Europe (south of the European ice sheet) and the Middle East, and advected cold, dry air deep into central Europe and Asia where the temperature was lowered by 20–30 K (Fig. 10) and precipitation was decreased (Fig. 14). The storm track shifted south and intensified (Fig. 13), but this was not accompanied by increased precipitation.

In the tropics, land temperature was generally lower (Fig. 10) and precipitation reduced (Fig. 14). As in July 18 kyr BP, there was a strong relationship between the prescribed sea surface temperature departures and simulated precipitation departures. For example, precipitation was reduced, compared to present, over most of the equatorial oceans where sea surface temperature was lower at 18 kyr BP than now; precipitation was increased over the western North Indian Ocean, the subtropical North and South Pacific and parts of the South Atlantic and South Indian Ocean where the sea surface temperature was prescribed to be warmer than now.

3) *9 kyr BP—July.* A striking feature of the simulation was the increased land surface temperature over the tropical and the northern continents and the in-

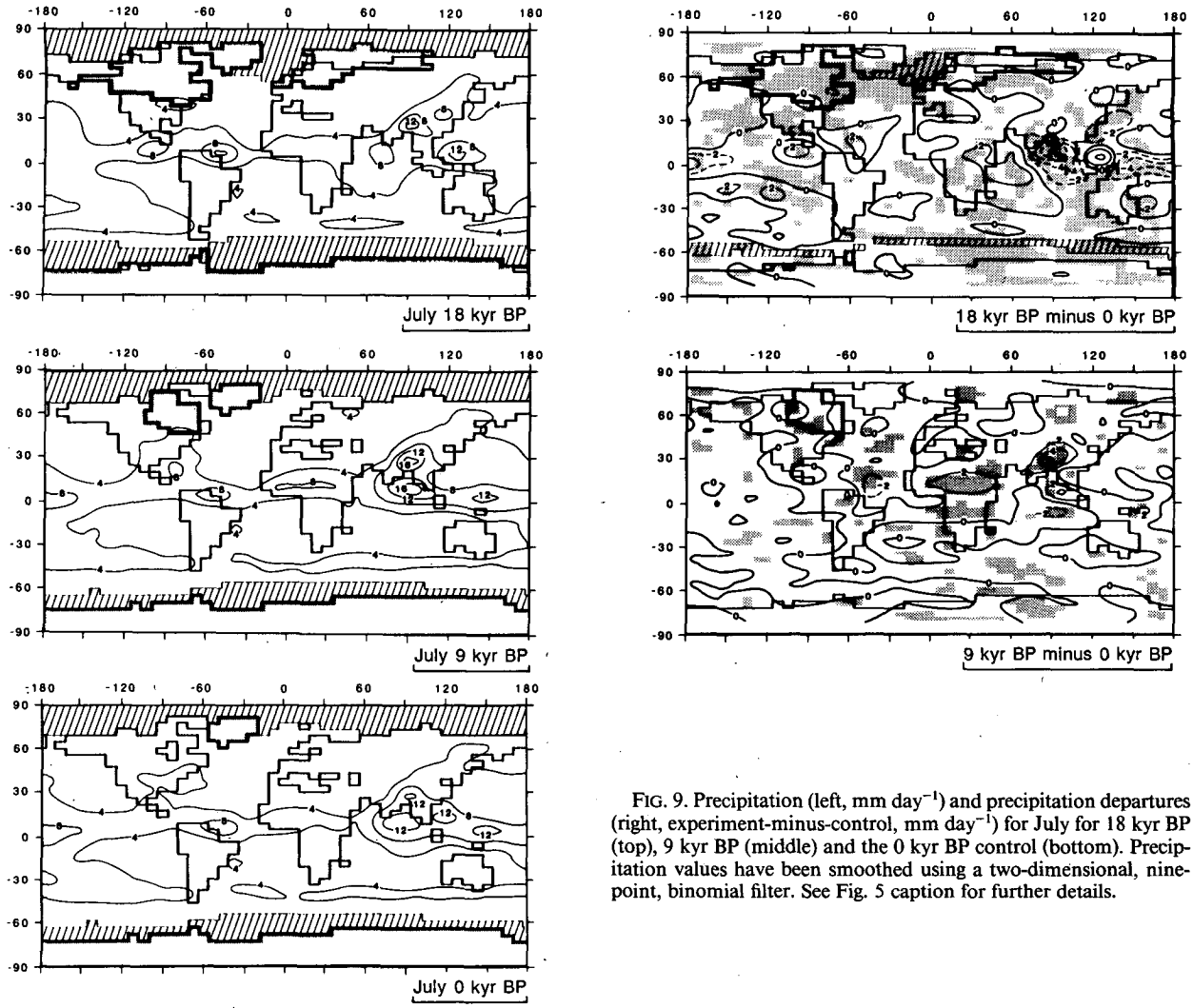

FIG. 9. Precipitation (left, mm day^{-1}) and precipitation departures (right, experiment-minus-control, mm day^{-1}) for July for 18 kyr BP (top), 9 kyr BP (middle) and the 0 kyr BP control (bottom). Precipitation values have been smoothed using a two-dimensional, nine-point, binomial filter. See Fig. 5 caption for further details.

tensification of the monsoon circulation. It was as much as 3–4 K warmer in central Asia and over 2.5 K warmer in parts of North Africa, Europe, Asia and North America (west, south and north of the remnant ice sheet) (Fig. 5). Sea level pressure was lowered by 3–6 mb across North Africa–south/central Asia and raised over the surrounding oceans (Fig. 6). The area of North Africa/Asia enclosed by the "1000-" and "1010-"mb contours was considerably larger at 9 kyr BP than it is at 0 kyr BP. There were strengthened southwesterlies extending farther north in west Africa and stronger Arabian Sea southwesterlies; the inflow of air over south and east Asia was generally stronger (Fig. 7). Over North Africa, the tropical easterly jet was stronger at 9 kyr BP than it is at 0 kyr BP (Fig. 7) by about 10 m s^{-1}. Precipitation was increased across North Africa, the Middle East, and south and east Asia, and, to a lesser extent, over most other land areas; precipitation decreased over the oceans where increased downward motion compensated for the increased upward motion over land (Fig. 9).

4) *9 kyr BP—January.* In January, the strongest monsoonal response to the decreased solar radiation occurred in the Southern (summer) Hemisphere. The temperature decreases of highest statistical significance were in the tropics. Land surface temperature was lowered, and sea level pressure was raised, over South America, tropical and South Africa, South Asia, and Australia (Figs. 10, 11). With the reduced intensity of the southern summer monsoon circulations, summer precipitation was decreased significantly over South America and South Africa (Fig. 14) and increased over the southern oceans. Similarly, upward vertical motion increased over the oceans and decreased over the land. In the western Indian Ocean, increased outflow of air from South Asia (Fig. 12) helped to enhance surface convergence and precipitation south of the equator.

Sea level pressure was increased over the remnant ice sheet in North America (Fig. 11), and weak ridging of the surface flow over the ice sheet (Fig. 12) advected warmer air from the west (Fig. 10). Sea level pressure was increased across North Africa–Southern Asia

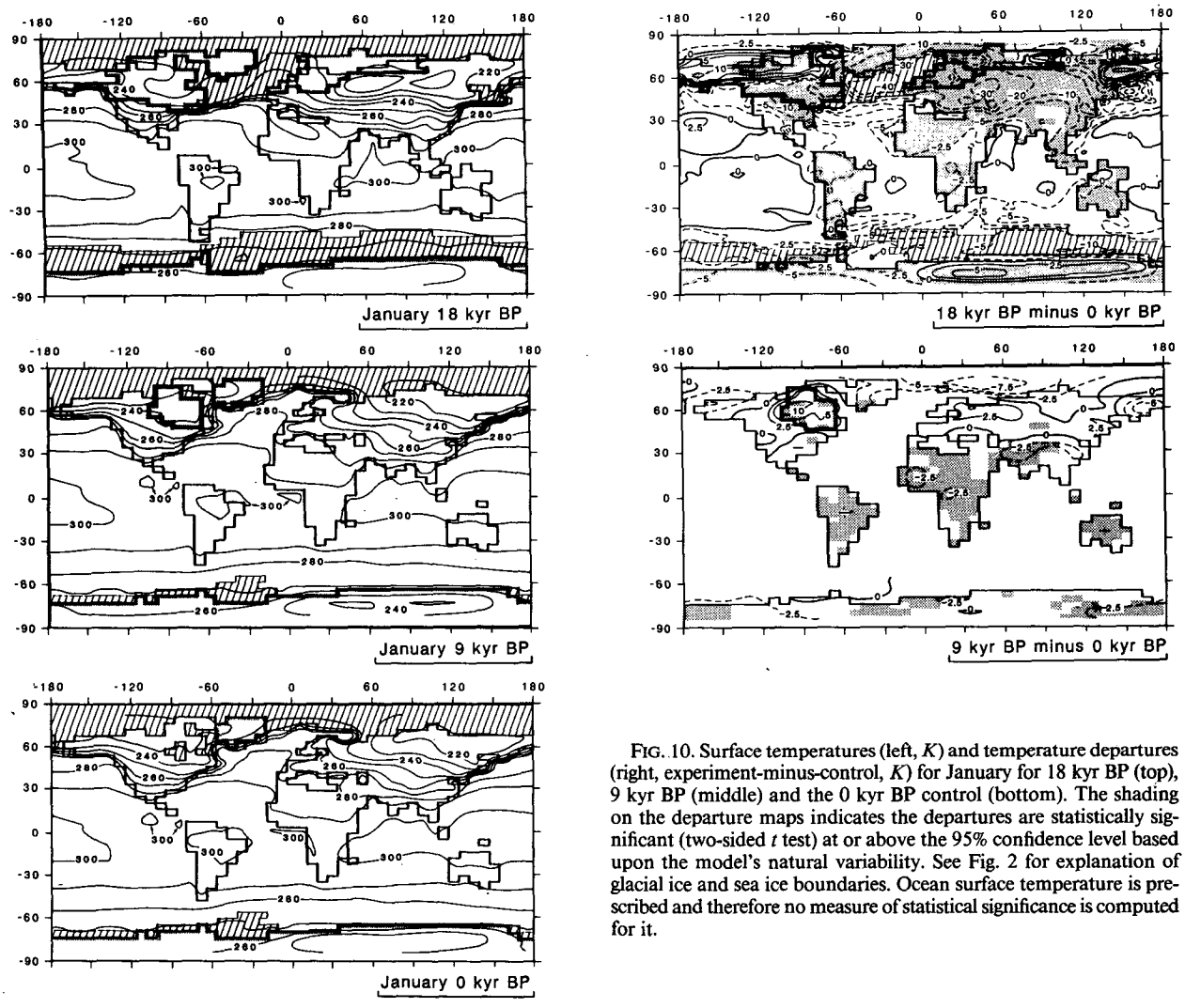

FIG. 10. Surface temperatures (left, K) and temperature departures (right, experiment-minus-control, K) for January for 18 kyr BP (top), 9 kyr BP (middle) and the 0 kyr BP control (bottom). The shading on the departure maps indicates the departures are statistically significant (two-sided t test) at or above the 95% confidence level based upon the model's natural variability. See Fig. 2 for explanation of glacial ice and sea ice boundaries. Ocean surface temperature is prescribed and therefore no measure of statistical significance is computed for it.

where temperatures were lowered. Along the northern flank of this strengthened anticyclonic cell, somewhat stronger midlatitude westerlies over the North Atlantic and western Europe caused warm air advection and a region of increased temperature in western Europe; however this feature was not statistically significant.

d. *Regional features*

We have summarized five regional features of the simulated climatic changes: i) the tropical monsoons of both hemispheres; ii) the northern midlatitude climates; iii) the surface climatic conditions for the northern ice sheets; iv) the tropospheric flow patterns in the vicinity of the northern ice sheets; and v) Northern Hemisphere land/ocean surface energy budgets.

1) *Tropical monsoons, 0–30°N and 0–30°S.* Perhaps the most striking result of the simulations was the strong response of the tropical monsoon systems to changes of the seasonal cycle of solar radiation; see Kutzbach and Street-Perrott, 1985, for more detailed results and comparisons with observations of past climates. Especially between 12 and 6 kyr BP, northern summer monsoons were stronger, associated with increased summertime radiation, and southern summer monsoons were weaker, associated with decreased summertime radiation. The summer precipitation increases were of order 20% in the band 0–30°N and the summer precipitation decreases were of order 20% in the band 0–30°S (Fig. 15). Increases in estimated annual $P - E$ were also large (Fig. 15), especially over North Africa and South Asia. Average wind vectors over land showed the strengthened southwesterlies in northern summer (0–30°N, July) from 15 to 6 kyr BP and winds with less northerly components in southern summer (0–30°S, January) at 12 and 9 kyr BP (Fig. 15).

Another feature of the precipitation departures was the large change in summer precipitation relative to winter precipitation (Fig. 15), although the radiative forcing changes were of similar magnitude in both seasons (Fig. 3a). These seasonal differences were due to

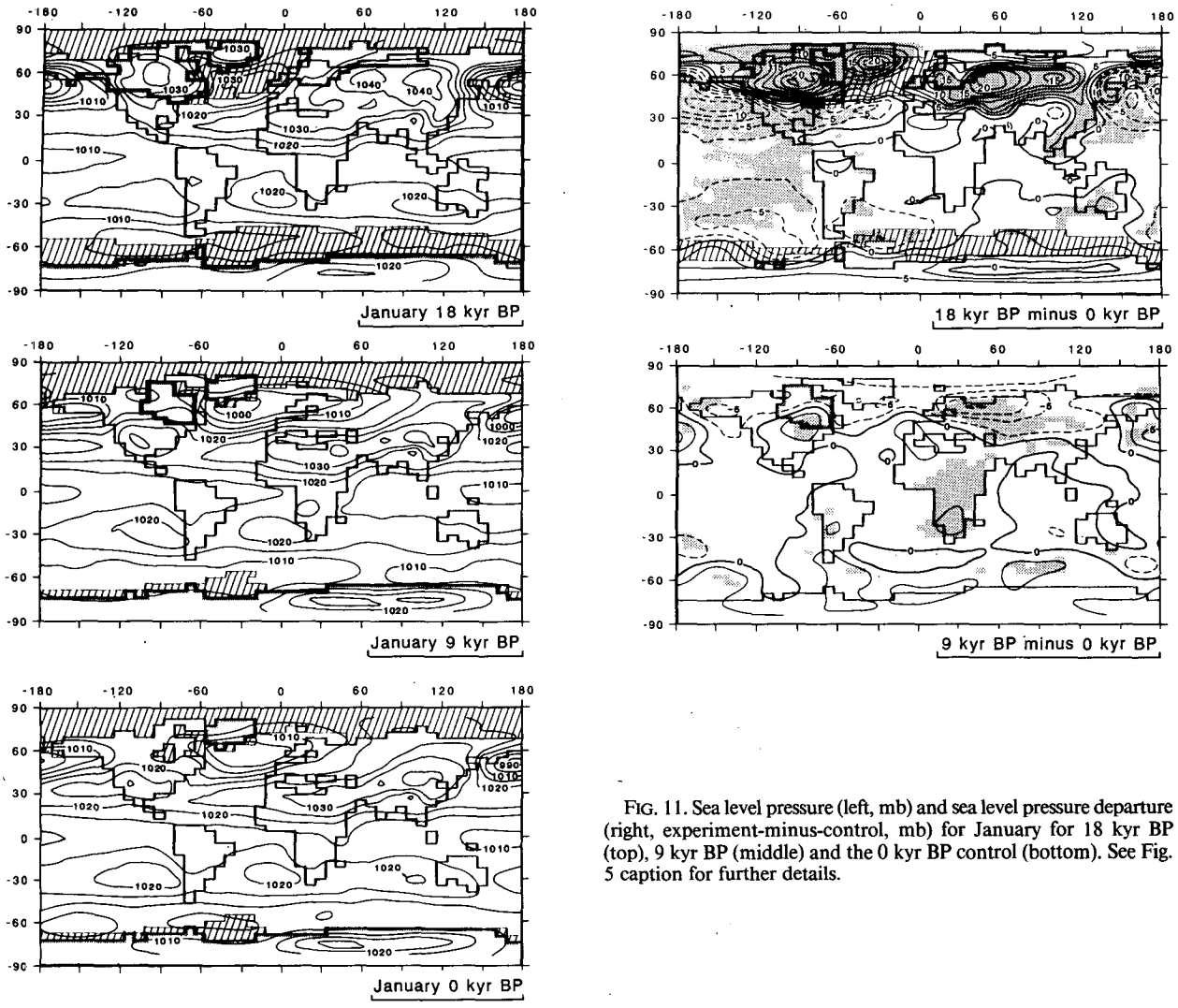

FIG. 11. Sea level pressure (left, mb) and sea level pressure departure (right, experiment-minus-control, mb) for January for 18 kyr BP (top), 9 kyr BP (middle) and the 0 kyr BP control (bottom). See Fig. 5 caption for further details.

a combination of dynamical and hydrological factors. These are summarized for the belt 0–30°N (Table 3). The dynamical factors, discussed earlier, were the differential warming or cooling of the land (relative to ocean) and the associated changes in the pressure distribution. For example, in July 9 kyr BP, the average surface temperature of the land was higher than that of the ocean (by 0.3 K) whereas it is lower (by −1 K) at 0 kyr BP. This warming of the land relative to the constant-temperature ocean (prescribed) was associated with a considerable strengthening of the sea level pressure difference between land and ocean; in the belt 0–30°N the pressure over land was 5.1 mb lower than over the ocean in July 9 kyr BP, compared to 2.5 mb lower in July 0 kyr BP. This was in turn associated with strengthened inflow and increased moisture convergence over land ($P - E$ = 2.1 mm day^{-1} at 9 kyr BP compared to 1.3 mm day^{-1} at 0 kyr BP). The flux of moisture from the Southern to the Northern hemisphere also increased at 9 kyr BP compared to 0 kyr BP.

In January, 0–30°N, these dynamical factors were less evident. The land temperature was considerably lower than the ocean temperature at 0 kyr BP (by 10.7 K) and, although this differential increased to 13 K at 9 kyr BP, the land–ocean sea level pressure differential (higher pressure over land) was only slightly larger at 9 kyr BP (7.3 mb) than at 0 kyr BP (5.9 mb), and there was no increase in moisture divergence over northern land (in fact, a slight decrease).

Added to the influence of these dynamical factors on the tropical monsoon climates were important changes in the local hydrologic and energy budgets that are similar to changes noted by Wetherald and Manabe (1975) in a solar constant sensitivity experiment with an atmospheric GCM coupled to a swamp ocean. Wetherald and Manabe found that a 6% increase in solar constant was accompanied by a 27% increase in evaporation and precipitation. This increase of evaporation and precipitation by a factor of 4.5 as compared to the increase in solar radiation was due to 1) the nonlinear increase of saturation vapor pressure with

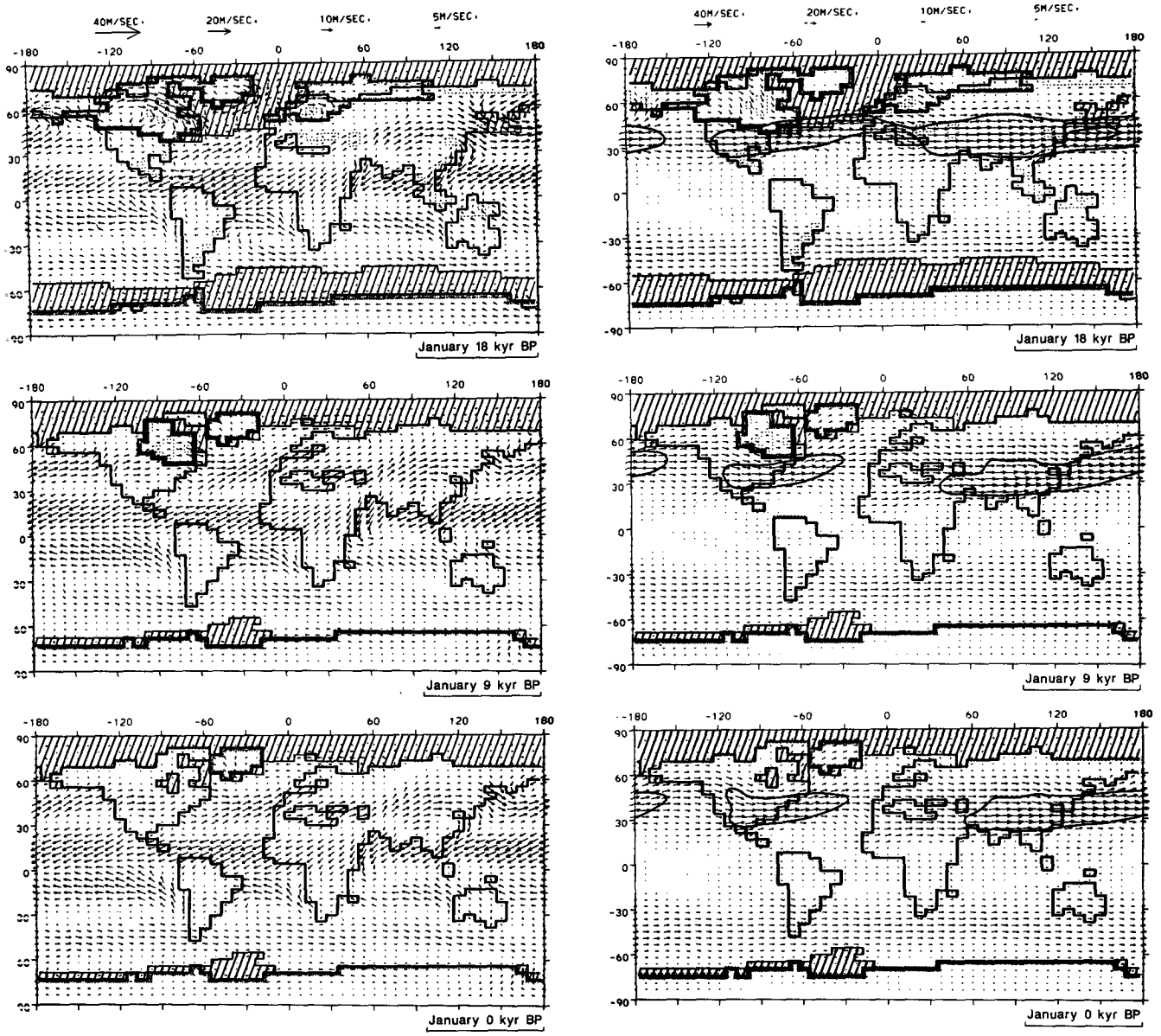

FIG. 12. Surface winds (left) and winds at sigma level 0.500 (right) for January. See Fig. 7 caption for details.

increasing temperature at the earth's surface; and 2) the decrease in the net upward longwave radiation related to increased moisture content of the atmosphere.

In the experiment for July 9 kyr BP, for the latitude belt 0–30°N (Table 3), we obtained a result similar to that of Wetherald and Manabe. The solar radiation at the top of the atmosphere was increased by 7%, the absorbed solar radiation at the surface increased by 6%, and the net longwave radiation loss decreased by 6% (even though the surface temperature was warmer). Net radiation increased by 11%. Evaporation increased by 14% whereas sensible heat flux increased by only 1%—an effective lowering of the Bowen ratio. The increased evaporation over land along with the increased moisture convergence over land from dynamical factors led to the 26% increase in precipitation, a factor of 3.7 times the percentage increase of solar radiation (comparing closely to the factor of 4.5 obtained by Wetherald and Manabe).

In January at 9 kyr BP, the net radiation at the surface decreased by 15%, but, associated with the considerably lower temperature, the sensible heat flux decreased 25% and the latent heat flux by only 11%. Precipitation did not decrease at all. For comparison, the corresponding values for 18 kyr BP are also listed in Table 3.

A somewhat more quantitative index of the sensitivity of precipitation to radiation changes and of the relative sensitivity of precipitation to radiation and glacial-age boundary condition changes was obtained

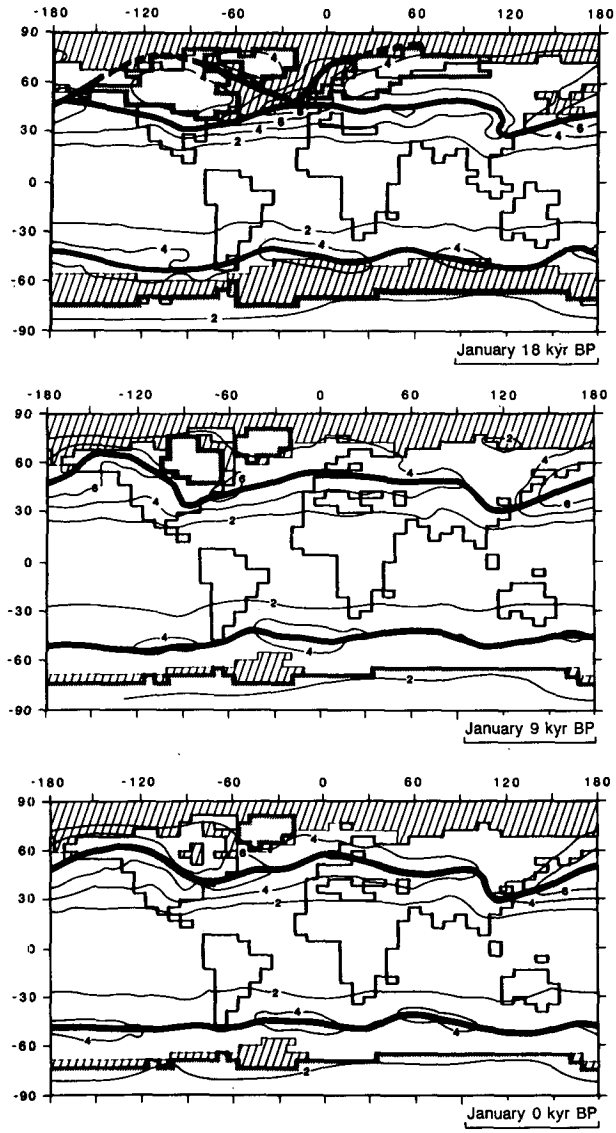

FIG. 13. Standard deviation of surface pressure (mb) for January for 18 kyr BP (top), 9 kyr BP (middle) and the 0 kyr BP control (bottom). The standard deviation is computed from the variance contained between periods of 2.5 and 6 days, using the band-pass filter described by Blackmon and Lau (1980). The shaded band indicates the latitude of relative maxima.

by plotting precipitation changes for each experiment, for various latitude bands and months, as a function of hemispheric-average solar radiation changes (Fig. 16). For land precipitation in the band 0–30°N in July, the linear slope (β) for the 0, 3 and 6 kyr BP experiments was about 3.5, indicating that a radiation change of 1% corresponded to a precipitation change of about 3.5% if there were no changes in lower boundary conditions. The experiments for 15 and 18 kyr BP, which included both orbital changes and the effect of CLIMAP-specified full-glacial boundary conditions, showed departures (δ) of about 0 and −3%, respectively, from the linear slope. These departures were within the plus/minus one-sigma range of the model's natural variability. Clearly, the number of cases are not sufficient to justify statistical estimation of the slope and departure parameters, but, whereas the positive relationship between $\Delta P/P$ (0–30°N, July) and $\Delta S/S$ is indicated for all experiments (Fig. 16), giving a maximum percentage increase of precipitation of about 28% for a solar radiation increase of about 8%, the percentage decrease of precipitation attributed to the glacial boundary conditions was at most 3% and was within the model's range of natural variability. A similar result ($\beta = 5$; $\delta = 0$ to 4%) was obtained for 0–30°S in January (Table 4). In winter, 0–30°N, January, and 0–30°S, July, the slope parameter (β) was much smaller—reflecting cooler conditions, lower levels of atmospheric moisture and reduced dependence of saturation vapor pressure on temperature (Table 4); however, as in summer, the effect of glacial boundary conditions remained small.

Another indication that orbital changes are relatively more important than glacial-age boundary condition changes for influencing tropical precipitation is gained from inspection of the time series of precipitation departure for July (0–30°N) and January (0–30°S); Fig. 15. Both curves are roughly symmetric around 9 kyr BP, quite like the radiation departure curves (Fig. 1, Fig. 3a), but unlike the changes of glacial-age boundary conditions which were confined (in the model) to the period from 18 to 9 kyr BP (Fig. 1).

In contrast to the results for the tropics, the cooler, nontropical portions of both hemispheres (30–90°N or 30–90°S) exhibited a comparatively small dependence of precipitation change on orbitally produced radiation change (smaller β's) but a large reduction of precipitation due to the glacial boundary conditions (δ's ranging from −15 to −20%) (see Table 4, Fig. 16, and subsection d3).

2) *Northern middle latitudes, 30–60°N.* Precipitation changes in nontropical latitudes differed from the changes in the tropics. There were also differences in the magnitude of temperature and evaporation changes, particularly in the ice-free continental interiors. In the latitude band 30–60°N, for ice-free regions only, the mid-Holocene July temperature maximum was especially well marked, along with the large depression of January temperature in the late glacial (Fig. 17). As in the northern tropics, July precipitation in northern midlatitudes was increased around 9 kyr BP. However, the increase was only about 10% (compared to 20% in the tropics). Moreover, evaporation increased more than the precipitation increased (the enhanced moisture convergence over land associated with increased monsoons did not penetrate to the midlatitude continental interiors) so that $P - E$ in the early-to-mid-Holocene (9 and 6 kyr BP) was below the 0 kyr BP level. The decreased $P - E$ of the band 30–60°N during this period contrasts with the tropical belt where the enhanced summer monsoon led to increased $P - E$. Put briefly, in the midlatitude northern lands,

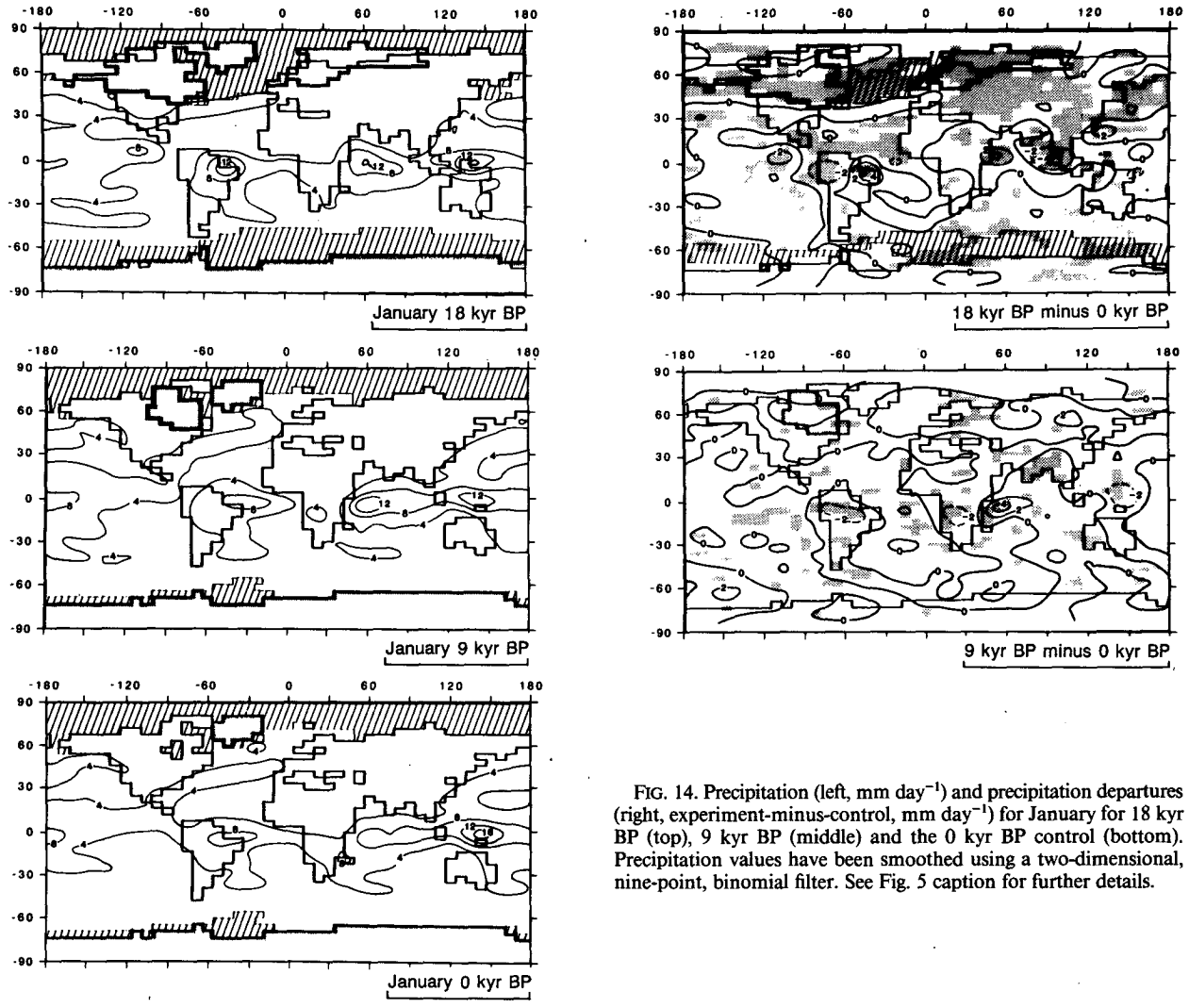

FIG. 14. Precipitation (left, mm day^{-1}) and precipitation departures (right, experiment-minus-control, mm day^{-1}) for January for 18 kyr BP (top), 9 kyr BP (middle) and the 0 kyr BP control (bottom). Precipitation values have been smoothed using a two-dimensional, nine-point, binomial filter. See Fig. 5 caption for further details.

especially the continental interiors of North America and Eurasia, the "cold–dry" glacial period was followed by a "warm–dry" early-to-mid-Holocene. Drier conditions south of the North American and Eurasian ice sheets were also noted in the 18 kyr BP simulation experiments of Manabe and Broccoli (1985).

3) *High northern latitudes: ice sheets.* For the regions of North America, Europe and Greenland covered with ice sheets at 18 kyr BP, three climatic indicators are summarized for the period 18 to 0 kyr BP: July surface temperature, estimated annual precipitation and $P - E$ (Fig. 18). At 18 and 15 kyr BP, these variables indicate conditions on the ice sheets whereas from 12 to 9 kyr BP for North America, and for 12 kyr BP for Europe they represent averages of ice-covered and ice-free surfaces. Thereafter, the North American and European regions are free of glacial ice.

July temperatures were well below freezing over all three ice sheets at 18–15 kyr BP, but had risen to near 0°C by 12 kyr BP. The absence of the European ice sheet after 12 kyr BP and the North American ice sheet after 9 kyr BP explains the rise of temperature to near 15°C.

For all three ice sheets, the estimated annual-average precipitation was reduced (compared to present) for the period 18 to 12 kyr BP (Fig. 18) when storm tracks were shifted far south. For the North American and European regions, the estimated annual-average $P - E$ was considerably higher at 18–12 kyr BP when the regions were ice covered than at 6–0 kyr BP when they were ice free. This was because the latent heat flux was reduced more than precipitation at 18–12 kyr BP.

In contrast with the model used by Manabe and Broccoli (1985), this version of the NCAR CCM doesn't distinguish between snow and rain, nor is there a snow budget equation. Therefore the results of these simulation experiments cannot be used to study the mass budgets for the North American and European ice sheets.

Changes of the July surface energy budget also reflect the fractional changes in area of the glacial ice (Fig. 18). For the North American area, net radiation was

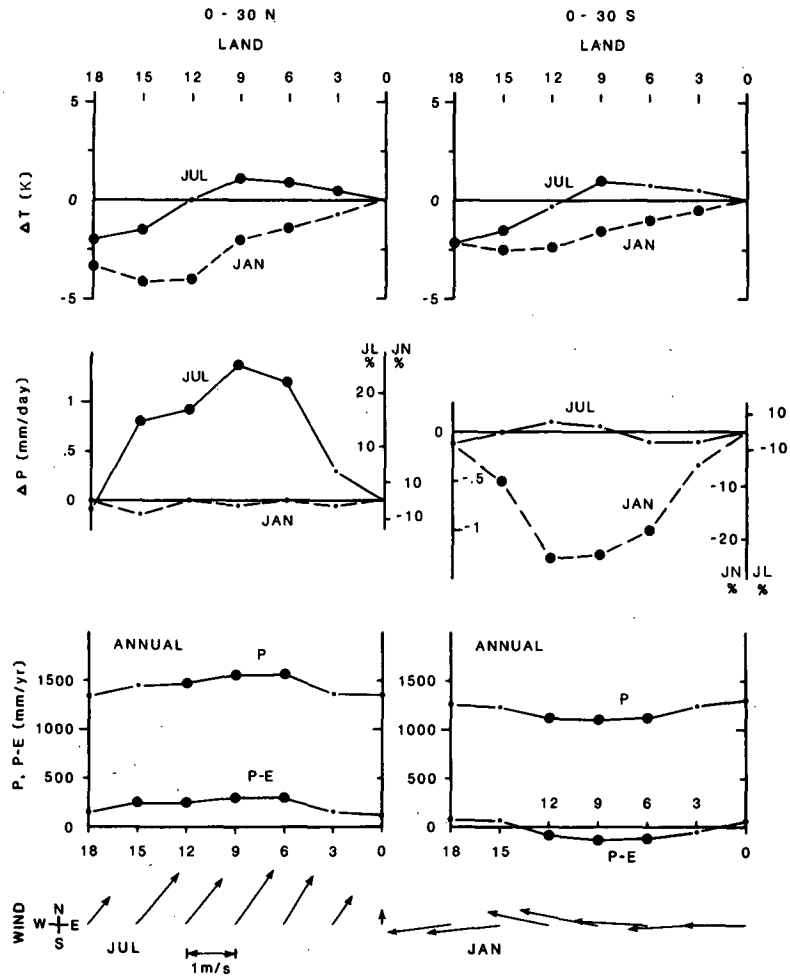

FIG. 15. Surface temperature departures for July and January (ΔT, K), precipitation departures for July and January (ΔP, mm day^{-1}), estimated annual precipitation and precipitation-minus-evaporation (P, $P-E$, mm yr^{-1}), and surface wind (July or January) for the land surface between 0–30°N (left) and 0–30°S (right). See Fig. 3b caption for further details.

near zero at 18–15 kyr BP when glacial ice covered the area. From 18 to 12 kyr BP the temperature at the first atmospheric level above the ice (sigma = 0.991, about 100 m) exceeded the temperature at the surface so that sensible heat was transfered to the surface and balanced the energy loss associated with latent heat flux. The approximate energy balance over the ice sheet at 18–15 kyr BP between sensible heat gain and latent heat loss is similar to results of Manabe and Broccoli (1985). The downward flux of sensible heat was a maximum at 9 kyr BP over the residual ice sheet (dashed line, Fig. 18). Two factors were probably involved: 1) the ice-free area (with low albedo) was larger at 9 than at 12 kyr BP, so that more warm air was available for advection over the small remnant ice sheet; and 2) the surrounding land was warmer at 9 kyr BP because of the increased solar radiation. With the removal of the ice from the area, the net radiation increased, the sensible heat flux reversed sign, and the latent heat flux increased.

4) *North American–European sector jets.* The mid-tropospheric westerly flow in January across the North American/North Altantic/European sector changed markedly from 18 to 0 kyr BP in response to the changes in ice-sheet and sea ice boundary conditions (Fig. 19). At 18 and 15 kyr BP, the flow was split around the North American ice sheet as discussed previously. At 12 kyr BP, the split flow was replaced by a more zonal flow over the ice sheet. The westerlies around 30°N over the eastern Pacific and southern USA were weaker than at 18–15 kyr BP. These changes between 18–15 kyr BP and 12 kyr BP must be attributed primarily to the decreased height of the ice sheet (maximum height of 3300 m at 18 kyr BP, 1650 m at 12 kyr BP). At 9 kyr BP (Fig. 12), with the height of the North American ice sheet reduced to 800 m, the ice

TABLE 3. Energy and hydrologic budget components (and percentage changes from present), and land/ocean temperature and pressure differences, for the latitude zone 0–30°N, 0, 9 and 18 *kyr* BP, July and January.

	July			January		
Parameter*	0 *kyr* BP	9 *kyr* BP	18 *kyr* BP	0 *kyr* BP	9 *kyr* BP	18 *kyr* BP
SW (top) (W m^{-2})	438	469 (7%)	441 (1%)	340	314 (−8%)	338 (−1%)
SW (net, surface) (W m^{-2})	222	236 (6%)	224 (1%)	178	162 (−9%)	177 (−1%)
LW (net, surface) (W m^{-2})	62	58 (−6%)	64 (3%)	77	76 (−1%)	78 (1%)
R (surface) (W m^{-2})	160	178 (11%)	160 (0%)	101	86 (−15%)	99 (−2%)
SH (W m^{-2})	40	41 (1%)	46 (15%)	28	21 (−25%)	32 (14%)
LH (W m^{-2})	120	137 (14%)	114 (−5%)	73	65 (−11%)	67 (−2%)
Tot. Cld. (fraction)	0.46	0.50	0.47	0.32	0.32	0.32
LH (mm/day)	4.1	4.7 (14%)	3.9 (−5%)	2.5	2.2 (−11%)	2.3 (−8%)
P (mm/day)	5.4	6.8 (26%)	5.4 (0%)	1.9	1.9 (0%)	1.9 (0%)
T (surface) (*K*)	299.3	300.5	297.3	287.3	285.5	283.9
ΔT ($L - O$) (*K*)	−1.0	+0.3	−1.5	−10.7	−13.0	−13.0
ΔSLP ($L - O$) (mb)	−2.5	−5.1	−3.2	5.9	7.3	7.2

* SW is short wave radiation; LW is long wave radiation; *R* is net radiation; SH is sensible heating; LH is latent heating; Tot. Cld. is total cloud; *P* is precipitation; *T* is temperature; ΔT is the difference in surface temperature between land (L) and ocean (O); ΔSLP is the difference in sea level pressure between land and ocean.

sheet caused only a weak ridging of the westerly flow. A major change of boundary conditions also occurred over the North Atlantic between 15 and 9 kyr BP when the sea-ice and ocean temperature were returned to their modern values. This was associated with a marked decrease in the strength of the North Atlantic westerlies. At 6–3 kyr BP the flow pattern was similar to the 0 kyr BP pattern.

The apparent sensitivity of the tropospheric flow patterns in the North American–North European sector to ice sheet height and North Atlantic sea-ice extension suggests that it is important to estimate these features quite accurately for paleoclimatic simulations.

The simulated changes in tropospheric flow patterns and storm tracks (Fig. 13) have features that support the discussions of Ruddiman and McIntyre (1981) concerning the role of extensions of North Atlantic sea-ice in shifting storm tracks (and precipitation) away from the North American ice sheet.

5) *Energy budget, cloud climatology—hemispheric averages, land-ocean contrasts (Table 5).* The large changes in solar radiation forcing at 9 kyr BP (due to orbital changes) and the large changes in absorbed solar radiation forcing at 18 kyr BP (due to albedo changes) provide an opportunity to compare and contrast the hemispheric-average response of surface energy and hydrologic budgets.

(i) *9 kyr BP.* For the Northern Hemisphere land, the imposed increase in solar radiation for July at the top of the atmosphere was 39 W m^{-2}. The increase in net solar radiation at the surface was 16 W m^{-2}. With the warmer land surface and the associated warming and increased moisture content of the atmosphere, the downward-directed longwave radiation increased and, therefore, the net longwave radiation loss was decreased by 3 W m^{-2}, producing a total increase in net radiation of 19 W m^{-2} at the land surface. Of the increased net radiation, 15 W m^{-2} was expended through increased evaporation. The precipitation increased by an amount of the same order of magnitude (in energy units) as the evaporation increase. Over the northern oceans, increased subsidence and radiative heating increased the near-surface stability, decreased evaporation, and, ultimately, decreased precipitation. The corresponding January changes were generally of opposite sign and smaller magnitude.

Changes in cloud cover occurred at several levels; in July there was an increased amount of high cloud and low cloud cover over the land (compared to present), and increased low cloud and decreased high cloud cover over the ocean. These cloudiness changes were consistent with increased rising motion and decreased stability over the land and increased sinking motion and increased stability over the ocean. Because of the vertical compensation of cloud cover changes over both land and ocean, the change in total cloud cover was about 1%. In January, the change in total cloud cover was near zero.

(ii) *18 kyr BP.* The incoming solar radiation differed only by 1–3 W m^{-2} from modern values, in contrast to 9 kyr BP. Changes in the radiation budget at the surface were nevertheless large, at least in July. The net solar radiation at the surface was reduced by 14 W m^{-2} over land, owing largely to increased surface albedo associated with prescribed changes of land ice and land albedo. The net longwave radiation loss from the surface increased by 7 W m^{-2}, associated with the drier atmosphere and reduced cloudiness. The combined effect was to decrease the net radiation by 21 W m^{-2} over land—a change of equal magnitude but opposite sign to that of July 9 kyr BP. Evaporation decreased by 16 W m^{-2}, comparable to the decrease in net radiation, and was associated with a decrease of precipitation of comparable magnitude. In contrast to the

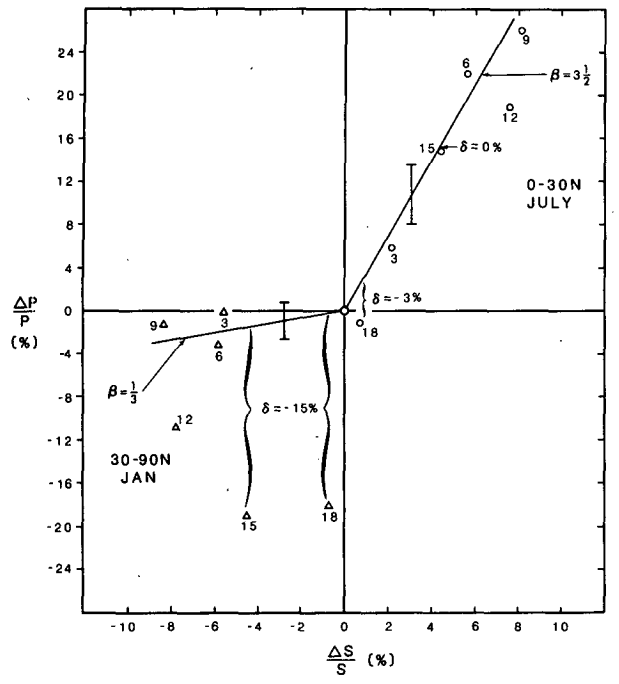

FIG. 16. Percentage change from present of precipitation over land ($\Delta P/P$) for the latitude bands 0–30°N in July (circles) and 30–90°N in January (triangles) as a function of percentage change of hemisphere-average radiation ($\Delta S/S$). The numbers (3, 6, . . . 15, 18) identify the experiment in kyr BP. The linear slope parameter (β) relating $\Delta P/P$ to $\Delta S/S$ is estimated by eye for the experiments 0, 3 and 6 kyr BP (orbital parameter changes and modern surface boundary conditions). The departures (δ) of the 15 and 18 kyr BP experiments (orbital parameter changes and CLIMAP-specified glacial boundary conditions) from the linear slope are marked with brackets. Vertical bars indicate the plus/minus one-sigma level of the model's natural variability for the latitude-average land precipitation for the 0 kyr BP control experiment. Values of β and δ for other months and latitude bands are as in Table 4.

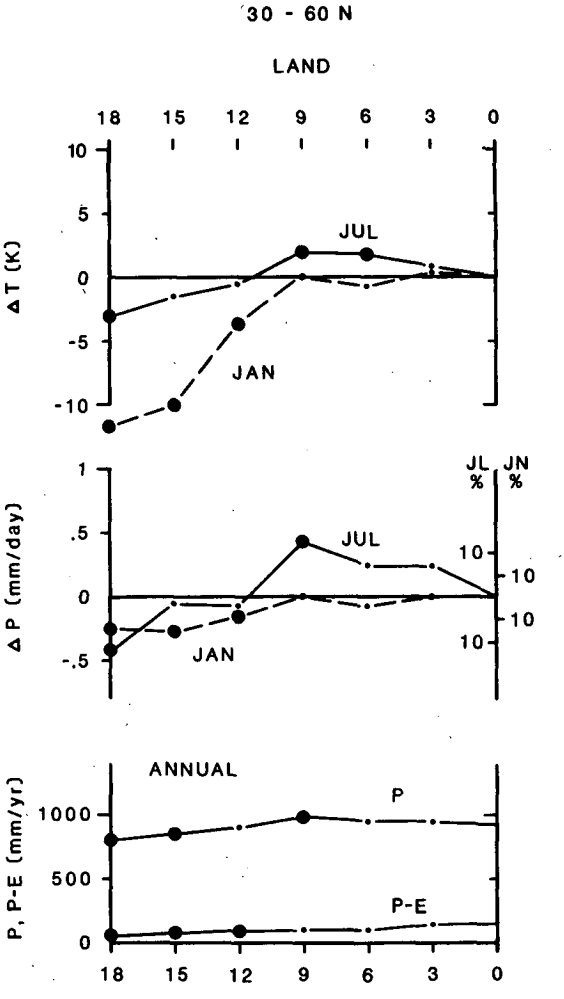

FIG. 17. As in Fig. 15 except for the ice-free land surface between 30–60°N.

situation at 9 kyr BP, the changes in evaporation and precipitation over the ocean were of the same sign and magnitude as the changes over land, owing to the CLIMAP-specified reductions in sea surface temperature and increases in land and sea-ice cover. The corresponding January changes were of similar sign but smaller magnitude.

Total cloud cover decreased by 1 to 2%, associated mainly with a decrease in low clouds, especially in July.

In summary, cloudiness feedback mechanisms did not play an important role in the simulated climatic changes. The relatively large changes in incoming solar radiation at the top of the atmosphere at 9 kyr BP (due to orbital changes) and in absorbed solar radiation at the surface at 18 kyr BP (due to surface albedo changes) produced relatively small changes in total cloudiness.

5. Summary of results

Both observational and model studies, summarized in sections 1 and 2, indicate the important role of

TABLE 4. Linear slope parameter (β) relating percentage changes from present of precipitation over land ($\Delta P/P$) to percentage change from present of hemisphere-average radiation ($\Delta S/S$) for experiments at 0, 3 and 6 kyr BP (orbital changes and modern surface boundary conditions); and, departures (δ) from the linear slope, in percent, of precipitation over land for the 15 and 18 kyr BP experiments (orbital-parameter changes and CLIMAP-specified glacial boundary conditions). See Fig. 16 and text for details. Values of β and δ are shown for July and January and for four latitude bands.

	90–30°N		30°N–0		0–30°S		30–90°S	
Month	β	δ(%)	β	δ(%)	β	δ(%)	β	δ(%)
July	2	−15, −20	3.5	0, −3	0	0, −5	0	−20
January	1/3	−15	2/3	−1, −3	5	0, 4	0	−10, −15

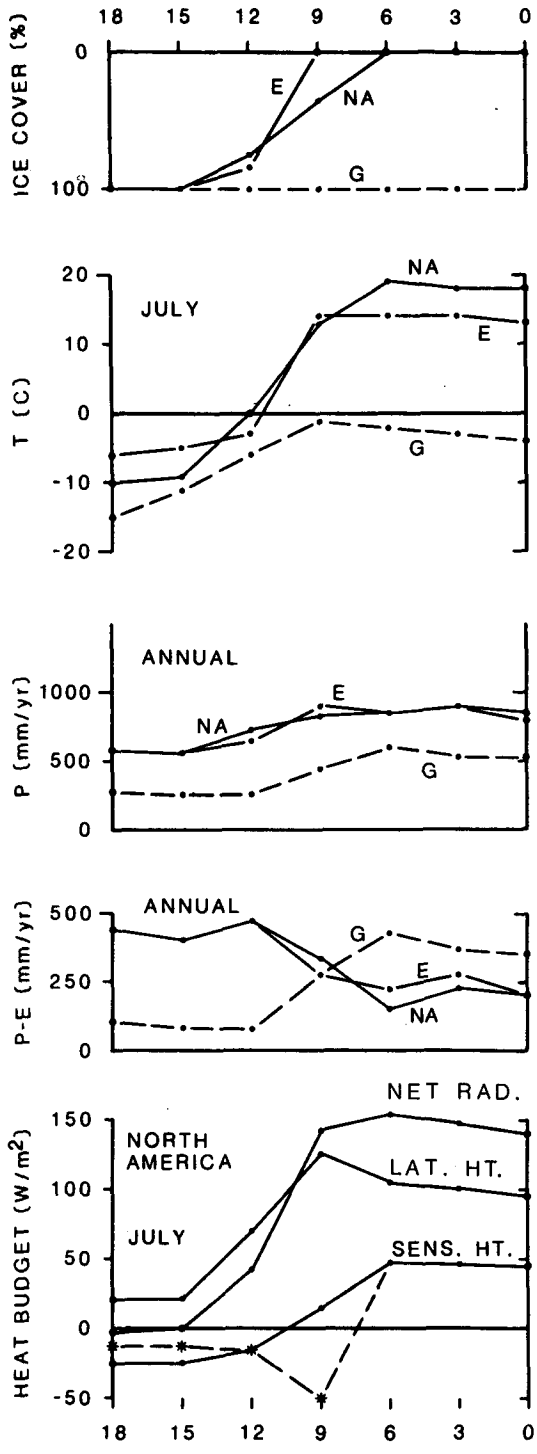

FIG. 18. Percentage of 18 kyr BP surface area covered with glacial ice for Europe (E), North America (NA) and Greenland (G) as a function of time (kyr BP), July surface temperature (°C), precipitation and precipitation-minus-evaporation (mm yr^{-1}) for estimated annual conditions; and components of surface energy budget for July for North America (net radiation, sensible heat, latent heat, in W m^{-2}). All values are averages for the area enclosed by the 18 kyr BP glacial ice limits in the respective regions; note that within this area there is no glacial ice in Europe after 12 kyr BP and in North America after 9 kyr BP. For sensible heat, the dashed line shows the value over glacial ice only.

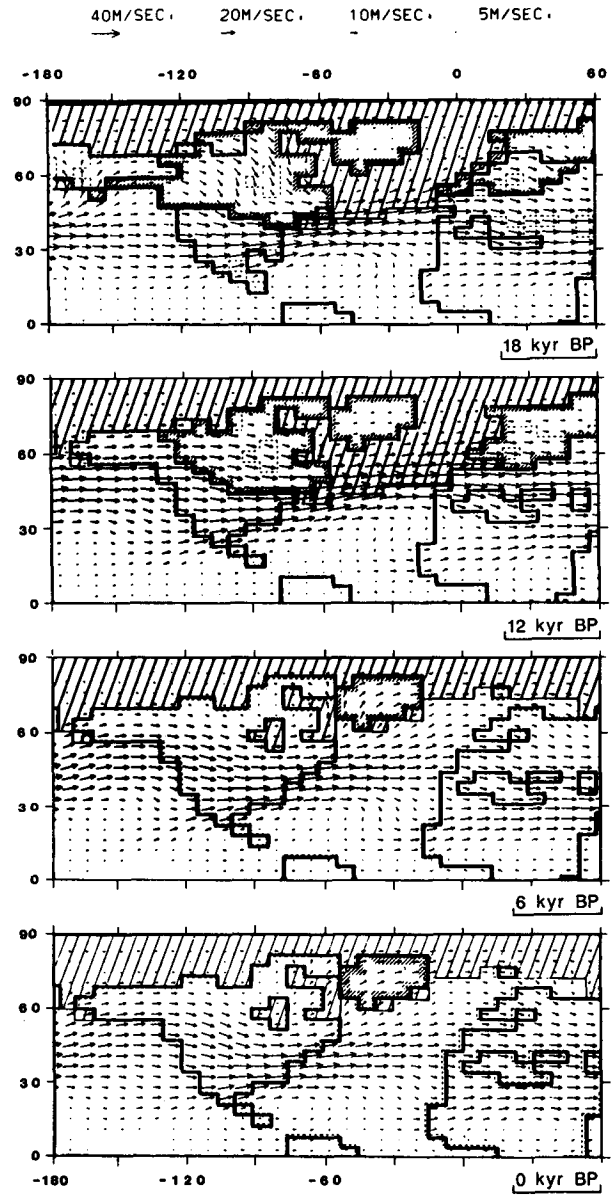

FIG. 19. Winds at sigma level 0.5 (about 500 mb or 5.5 km) for January for 18 kyr BP (top), 12 kyr BP and 6 kyr BP (middle) and 0 kyr BP (bottom) for the sector 0°–90°N and 180°W–0°. Arrows at top indicate scaling of wind magnitude.

changes of earth's orbit in causing major climatic changes of the past several hundred thousand years. Going beyond most previous studies with global or zonal-average climate models, this study and our previous AGCM simulations of the 9 kyr BP climate help to clarify at least three interrelated mechanisms whereby the orbital variations influence the climate: the variations in the seasonal radiation cycle produce changes in the seasonal temperature cycle; the different thermal properties of land and ocean lead to changes in continent-scale monsoon circulations; and the nonlinear relationship between temperature and saturation

TABLE 5. Radiation and surface energy and hydrologic budget changes, and cloudiness changes, for July and January for the Northern Hemisphere land (L), ocean (O), and land plus ocean ($L + O$). Abbreviations are the same as in Table 3.

Variable	July			Jan.		
	$L+O$	L	O	$L+O$	L	O
			9000 yr BP minus modern			
ΔSW, top (W m^{-2})	37	39	34	−18	−15	−22
ΔSW, surface (W m^{-2})	17	16	18	−12	−9	−15
ΔLW, surface (W m^{-2})	−3	−3	−3	0	0	0
ΔR, surface (W m^{-2})	20	19	21	−12	−9	−15
ΔE (W m^{-2})	1	15	−7	2	−4	6
ΔE (mm day^{-1})	0.07	0.47	−0.19	0.08	−0.13	0.20
ΔP (mm day^{-1})	0.17	0.71	−0.18	0.05	−0.02	0.10
Tot. Cld. 9 kyr BP	0.46	0.44	0.47	0.35	0.34	0.36
Tot. Cld. 0 kyr BP	0.45	0.43	0.46	0.35	0.34	0.36
Tot. Cld. Δ	0.01	0.01	0.01	0.00	0.00	0.00
			18 000 yr BP minus modern			
ΔSW, top (W m^{-2})	3	3	3	−2	−1	−2
ΔSW, surface (W m^{-2})	−6	−14	−1	−2	0	−3
ΔLW, surface (W m^{-2})	6	7	6	0	4	−2
ΔR, surface (W m^{-2})	−12	−21	−7	−2	−4	−1
ΔE (W m^{-2})	−11	−16	−8	−5	−2	−7
ΔE (mm day^{-1})	−0.38	−0.55	−0.27	−0.16	−0.06	−0.23
ΔP (mm day^{-1})	−0.42	−0.34	−0.46	−0.20	−0.19	−0.20
Tot. Cld. 18 kyr BP	0.43	0.41	0.44	0.34	0.32	0.36
Tot. Cld. 0 kyr BP	0.45	0.43	0.46	0.35	0.34	0.36
Tot. Cld., Δ	−0.02	−0.02	−0.02	−0.01	−0.02	0

vapor pressure causes large variations in the hydrologic cycle to occur in summer and in tropical latitudes. These mechanisms are briefly summarized below.

1) Changes of the date or season of perihelion cause major changes in the seasonal radiation cycle, and, in turn, the seasonal cycle of surface temperature. These seasonal temperature changes are of the order of several degrees Kelvin in continental interiors at low, middle and high latitudes. The increased axial tilt, a maximum around 9 kyr BP, further enhances the summer warming and winter cooling in the Northern Hemisphere.

2) The different thermal properties of land and ocean lead to much larger temperature changes for the continents than for the oceans. Thus, the zonally symmetric changes in the seasonal cycle of solar radiation are transformed into continent-scale adjustments of the temperature and pressure fields and the monsoon circulations. Whereas much of the previous work on the Milankovitch theory of climatic change emphasized the radiation and climatic changes in high latitudes (for example, see Imbrie and Imbrie, 1979), our results show that changes in continent-scale monsoon circulations of the tropical and midlatitudes, associated with the differential response of land and ocean, are an important component of the overall climatic response to orbital forcing. Summer monsoon precipitation changes over tropical lands are of order 10–20%. Changes of this magnitude are consistent with evidence from the geologic record (Kutzbach and Street-Perrott, 1985) and are well above the model's level of natural variability.

3) The nonlinear relationship between temperature and saturation vapor pressure causes the simulated changes of tropical precipitation to be much larger in the summer seasons of both hemispheres than in winter—even though the solar radiation changes are of comparable magnitude in both seasons. Likewise, the sensitivity of precipitation changes to radiation changes is weaker at higher (cooler) latitudes than in the tropics. This mechanism, along with temperature-dependent changes in evaporation, produces significant changes in annual precipitation-minus-evaporation without necessarily producing changes in annual temperature.

Consistent with results of previous studies (sections 1 and 2) the simulation for 18 kyr BP with the NCAR CCM shows that the boundary conditions specified by CLIMAP Project Members (1981) for glacial ice, sea ice, ocean surface temperature, and land albedo produce major changes in atmospheric circulation. Moreover, persistent glacial-age features, such as the North American ice sheet, continued to exert a strong influence on the Northern Hemisphere circulation until at least 9 kyr BP. Nevertheless, the results of Kutzbach and Street-Perrott (1985) and of this study show that the general response of tropical monsoon circulations to the orbitally produced solar radiation changes is much larger than their response to changes of long time-constant glacial-age boundary conditions. The reverse holds in nontropical latitudes.

Several results for broad area-averages appear to be in general agreement with the geologic record: 1) the warmer summers of mid- and high-latitude northern

lands (except near ice sheets) during deglaciation (12–9 kyr BP), the maximum summer warmth (Northern Hemisphere) around 6 kyr BP when the increased July radiation was still quite significant and the American and European ice sheets were gone, and the subsequent trend toward cooler summers; 2) the wetter conditions in the northern tropical lands between 12 and 6 kyr BP, associated with stronger monsoons and caused by the increased seasonality of solar radiation in the Northern Hemisphere; and, 3) the drier (as well as warmer) summers in northern midlatitude (ice-free) lands during the same period, 12 to 6 kyr BP, when evaporation increased more than precipitation.

In addition to the results obtained for broad area-averages, the experiments also produced rather detailed spatial patterns of climate that are in agreement with geologic records. For example, at 18 kyr BP over North America the southward-displaced jet and storm track were associated with cool and moist conditions in parts of the U.S. Southwest (in agreement with evidence; Kutzbach and Wright, 1985). Also, in agreement with simulations by Manabe and Broccoli (1985) and with geologic evidence, the regions south of both the North American and European ice sheets were dry. At 12 to 6 kyr BP, the spatial pattern of increased precipitation across North Africa and South Asia agrees closely with the regional distribution of sites where lake-levels were high (Kutzbach and Street-Perrott, 1985).

Several of the results suggest potentially significant features of climatic change that are not well documented in the literature. Further analysis of the geologic record is needed to test these features of the simulations. In this category are 1) the weaker Southern Hemisphere monsoons (and cooler, drier conditions) between 12 and 6 kyr BP; 2) the delayed summer warming of Southern Hemisphere lands (9 to 0 kyr BP, January) in contrast to the early warming trend (18 to 9 kyr BP, July) for the northern lands; 3) the split flow pattern around the North American ice sheet at 18 kyr BP, and the subsequent flow changes, especially between 15 and 12 kyr BP, as the ice sheet became smaller in area and height; 4) the westerly flow along the northern flank of the ice sheets in the 18 and 15 kyr BP simulations that replaced the modern polar easterlies and thus produced a major directional change in the winds over the Arctic Ocean; 5) the southward shift of the Southern Hemisphere westerlies in winter (July), 18–15 kyr BP; and 6) the approximate uniform value of global and annual-average temperature from 9 to 0 kyr BP.

This last point deserves somewhat more extensive comment because of its potential relevance to so-called "warm-earth scenarios" associated with increased levels of CO_2 (Kellog, 1978). The Northern Hemisphere evidence of the "Hypsithermal" (Kellog, 1978) may be primarily evidence of summer warmth and annual-average temperatures may have been much the same as now (Webb, 1985). If this is so, then the usefulness of the climate of this period as a possible scenario or analog of a CO_2-caused warm earth is questionable, since increased CO_2 levels would presumably produce warming in all seasons and hence a higher annual-average temperature.

Although this paper has focused on climatic changes of the past, some results are of interest for studies of modern climate as well. The seasonal radiation cycle of 9 kyr BP approximates a sensitivity experiment on the amplitude of the modern seasonal radiation cycle. The climatic response to the zonally symmetric changes of solar radiation produced by the different thermal properties of land and ocean clearly delineates the continent-wide scale of the North Africa-Eurasia monsoon and, of lesser magnitude, the North American, South American, and South African monsoons; also, the simulations further illustrate the relation between continent size and the magnitude of the seasonal temperature range (North et al., 1983). Another feature of the seasonal (monsoonal) sensitivity is a general tendency for east–west adjustments of opposite sign over land and ocean. Thus, for example, at 9 kyr BP and for 0–45°N, lower pressure, increased upward motion and increased precipitation occurred over land and increased pressure, decreased upward motion and decreased precipitation occurred over ocean. As a result of this tendency, changes in the zonal-average Hadley circulation are relatively small, whereas changes in regional "Hadley" cells and east–west (land–ocean) cells are relatively large.

The examples of apparent good agreement between the computed paleoclimate and the actual climatic record (Kutzbach and Street-Perrott, 1985; Kutzbach and Wright, 1985) suggest that the NCAR CCM is capable of simulating certain features of climate change rather accurately over a significant range of input parameters. The good agreement also indicates that it may be possible to estimate the contribution of orbital parameter changes to climatic changes of the next few millenia.

Certain of the results are no doubt dependent on the choice of model and prescribed boundary conditions, and differences are to be expected if and when similar experiments are performed with other models, with different versions of the NCAR CCM, or with different prescribed boundary conditions (Appendix). An example of possible model-dependence of these results is the known bias of the NCAR CCM toward winters that are colder than observed; this bias could influence the sensitivity of wintertime precipitation to orbitally produced radiation changes. Concerning prescribed conditions, the large changes in climate produced by changes in area of sea ice and height of land ice suggest that these relatively poorly known features of the glacial-age climate can strongly influence regional results.

Models with interactive ice sheets, oceans, land surface and biosphere will ultimately be needed to study in greater detail the mechanisms whereby a more complete climate system responds to orbital forcing.

Acknowledgments. Research grants to the University of Wisconsin-Madison from the National Science Foundation's Climate Dynamics Program (Grants ATM-8219070 and ATM-8412958) supported this work. The computations were made at the National Center for Atmospheric Research (NCAR), which is sponsored by the National Science Foundation, with a computing Grant 35381017 from the NCAR Computing Facility. The authors thank Warren Washington (NCAR) for help and advice in the use of the NCAR Community Climate Model, Mary Sternitzky for preparing the manuscript, Bryan Richards, Pat Behling and Mary Meyer for preparing the illustrations, and Thompson Webb III for reading the draft manuscript and suggesting improvements. J.E.K. acknowledges with thanks the opportunity to be a Summer Visitor to the AAP Climate Section, NCAR, August 1984 and 1985.

APPENDIX

Additional Experiments

A number of improvements in the model simulations are planned or completed, and these are summarized here.

1. Full seasonal cycle

We have made seasonal cycle simulations for 9 kyr BP with a low-resolution AGCM (Kutzbach and Otto-Bliesner, 1982) and with a version of the NCAR CCM that also included variable soil moisture and snow cover (see section 2). In both of these experiments, the June/July/August, December/January/February, and annual-average results correspond closely with the July, January, and estimated annual results that we obtained from the perpetual July and January experiments. That is, the perpetual July and January experiments do not appear to have seriously exaggerated the seasonal extremes and hence the sensitivity to orbital parameter changes. Based upon this comparison of perpetual and seasonal-cycle experiments for 9 kyr BP, we expect that the results obtained from the perpetual January and July experiments for 12 and 6 kyr BP would not be altered significantly if based upon full seasonal cycle experiments. However, at times when perihelion was closer to the vernal equinox (18 and 15 kyr BP) or the autumnal equinox (3 kyr BP), it would be of particular importance to study full seasonal simulations.

2. Variable soil moisture and snow cover

We have completed experiments for 9 kyr BP and 0 kyr BP with a version of the NCAR CCM that includes variable soil moisture and snow cover. The model is identical to that used in certain CO_2 sensitivity experiments (Washington and Meehl, 1984) except that the seasonal cycle of sea surface temperature and sea ice was prescribed. The simulated climatic changes for tropical lands at 9 kyr BP with variable soil moisture were closely comparable to those simulated with fixed soil moisture (Table 6a). In northern midlatitude lands, the increased warmth and aridity at 9 kyr BP was more pronounced with the variable soil moisture model. We have not assessed the feedback effect of snow-cover changes on the simulated 9 kyr BP climate. We intend to repeat the full set of experiments with a model that has these and other improvements.

3. Mixed-layer ocean/sea ice

A key assumption in the experiments with prescribed sea surface temperature is that the primary thermal response of the ocean to the altered seasonality of the solar radiation forcing will be small compared to the response of the land surface (see section 2a, also Kutzbach and Otto-Bliesner, 1982; Schneider and Thomson, 1979). This assumption is supported by field evidence (Ruddiman and Mix, Prell, personal communication, 1985) that the world's oceans had near

TABLE 6. Changes in land surface temperature (ΔT_s), precipitation (ΔP), and precipitation-minus-evaporation $\Delta(P - E)$, expressed as departures of experiment from the 0 kyr BP control for (a) land between 0 and 30°N, 9 kyr BP minus 0 kyr BP, for models with fixed variable soil moisture; (b) Northern Hemisphere land, 18 kyr BP minus 0 kyr BP, for models with CO_2 concentration set at 330 ppmv and 200 ppmv.

Variable	Jul	Jan	Est. Ann.	JJA	DJF	Ann.
(a) Land, 0 to 30°N, 9 kyr BP–0 kyr BP						
	Fixed soil moisture			Variable soil moisture		
ΔT_s (K)	1.2	−1.9	−0.6	1.6	−3.0	−0.7
ΔP (mm day^{-1})	1.4	−0.0	0.6	1.3	−0.5	0.3
$\Delta(P - E)$ (mm day^{-1})	0.8	0.3	0.5	1.0	0.1	0.4
(b) Northern Hemisphere land, 18 kyr BP–0 kyr BP						
	CO_2—330 ppmv			CO_2—200 ppmv		
ΔT_s (K)	−5.9	−6.6	−6.5	−6.1	−6.9	−6.7
ΔP (mm day^{-1})	−0.34	−0.19	−0.28	−0.42	−0.22	−0.34
$\Delta(P - E)$ (mm day^{-1})	0.21	−0.13	0.04	0.15	−0.14	0.01

modern temperatures by 9 kyr BP except near upwelling zones along continental boundaries (for example, in the Arabian Sea; Prell, 1984).

Nevertheless, we are beginning a series of experiments with the CCM coupled to a mixed-layer ocean for two reasons. First, as shown by Schneider and Thompson (1979), the interactions between the seasonally varying insolation and seasonally and latitudinally varying albedo and latitudinally varying ocean thermal inertia can cause a nonzero global annual temperature residual even if the annual insolation is unchanged. Second, our experiments show that the orbital parameter changes caused large changes of the circulation that may further perturb the surface energy budget over the ocean and produce additional feedback.

TABLE 7. Surface temperature (T_{sfc}), precipitation and evaporation actual or percentage changes from present, for selected area-averages for (a) July and (b) January 0, 9 and 18 kyr BP: *G, L + O* (global, land plus ocean); NH, *L* (Northern Hemisphere, land), etc. Changes significant above the 95% level are underlined.

Variable	Space average	0 kyr BP	9 kyr BP (% or Δ change)	18 kyr BP (% or Δ change)
	July			
T_{sfc} (K)	*G, L + O*	288.9	0.3	−3.9
	NH, *L*	293.8	1.1	−5.9
	NH, *L*, 0–30°N	299.3	1.3	−1.9
	SH, *L*, 0–30°S	289.6	1.0	−2.2
	SH, *L*	268.9	0.8	−0.9
Precipitation (mm day^{-1})	*G, L + O*	3.9	2%	−7%
	NH, *L*	4.0	18%	−9%
	NH, *L*, 0–30°N	5.4	26%	−1%
	SH, *L*, 0–30°S	1.7	5%	−6%
	SH, *L*	1.6	4%	−12%
Evaporation (mm day^{-1})	*G, L + O*	3.9	2%	−7%
	NH, *L*	3.5	13%	−15%
	NH, *L*, 0–30°N	4.1	14%	−5%
	SH, *L*, 0–30°S	2.7	10%	−9%
	SH, *L*	1.9	8%	−9%
	January			
T_{sfc} (K)	*G, L + O*	283.7	−0.3	−3.7
	NH, *L*	261.6	−0.5	−6.6
	NH, *L*, 0–30°N	287.3	−1.8	−3.4
	SH, *L*, 0–30°S	299.9	−1.5	−2.1
	SH, *L*	286.1	−1.6	−1.8
Precipitation (mm day^{-1})	*G, L + O*	3.6	2%	−3%
	NH, *L*	1.7	−1%	−11%
	NH, *L*, 0–30°N	1.9	−0%	−0%
	SH, *L*, 0–30°S	5.5	−23%	−2%
	SH, *L*	3.9	−21%	−4%
Evaporation (mm day^{-1})	*G, L + O*	3.6	2%	−3%
	NH, *L*	1.2	−10%	−5%
	NH, *L*, 0–30°N	2.5	−11%	−8%
	SH, *L*, 0–30°S	4.3	−10%	−6%
	SH, *L*	3.1	−10%	−6%

Since both the model results and marine geologic evidence point toward significant changes of coastal wind patterns (for example, in the Arabian Sea at 9 kyr BP) it would be desirable to include oceanic upwelling in the experiments. As an initial step, experiments by Prell, O'Brien and Luther (personal communication, 1985) are using simulated winds from the 9 kyr BP experiments to drive an ocean upwelling model. Further experimentation will also involve the use of coupled atmosphere/dynamical ocean models. By using coupled atmosphere–ocean models, the ocean surface boundary conditions would not be prescribed, therefore permitting paleoclimatic information from the ocean to be used for verification (Manabe and Broccoli, 1985).

4. Influence of CO_2 and late-glacial aerosol

Large changes of atmospheric CO_2 concentration and aerosol loading are inferred from the climatic record [Fig. 1 and section 3c (2)] and should be included in future experiments. Manabe and Broccoli (personal communication, 1985) used a lowered concentration of CO_2 at 18 kyr BP in experiments with an atmosphere/mixed layer ocean model. We completed experiments for 18 kyr BP (January and July) with CO_2 concentration set at 200 ppmv and with other 18 kyr BP boundary conditions prescribed as summarized in section 3. As might be anticipated, the effect of the CO_2 reduction on the climate over the oceans was rather small because SST's and sea ice were prescribed from CLIMAP. Over land, however, there was a small additional lowering of surface temperature and a decrease of precipitation and precipitation-minus-evaporation, compared to the 18 kyr BP experiment with CO_2 concentration of 330 ppmv (Table 6b). The results with the lower CO_2 concentration were in slightly better agreement with observations in the northern tropics (Kutzbach and Street-Perrott, 1985).

5. Episodic events in the climatic record

The climatic record contains ample evidence of climatic events that occur on shorter time-scales than considered here. One such event, the so-called "Younger Dryas," occurred around 10.5 kyr BP. This period of apparently worldwide climatic change lasted for less than a thousand years and was superimposed on the general postglacial climatic trend (Porter, 1981; Street-Perrott and Roberts, 1983; Ruddiman and McIntyre, 1981). Although our simulations agree fairly well with the broad evolution of global climates since the last glacial maximum, there remains a rich spectrum of climatic fluctuations on time scales ranging from decades to millenia that are not simulated by the approaches used here.

6. Tabular results

Table 7 summarizes the surface temperature, precipitation, and evaporation changes for various areas for 0, 9 and 18 kyr BP.

REFERENCES

Alyea, F. N., 1972: *Numerical Simulation of an Ice Age Paleoclimate.* Atmos. Sci. Paper No. 193. Colorado State University, 120 pp.

Berger, A. L., 1978: Long-term variations of caloric solar radiation resulting from the earth's orbital elements. *Quat. Res.*, **9**, 139–167.

Birchfield, G. E., J. Weertman and A. T. Lunde, 1981: A paleoclimate model of Northern Hemisphere ice sheets. *Quat. Res.*, **15**, 126–142.

Blackmon, M. L., and N. C. Lau, 1980: Regional characteristics of the Northern Hemisphere wintertime circulation: A comparison of the simulation of a GFDL general circulation model with observations. *J. Atmos. Sci.*, **37**, 497–513.

——, J. E. Giesler and E. J. Pitcher, 1983: A general circulation model study of January climate anomaly patterns associated with interannual variation of equatorial Pacific Sea surface temperatures. *J. Atmos. Sci.*, **40**, 1410–1425.

Chervin, R. M., and S. H. Schneider, 1976: On determining the statistical significance of climate experiments with general circulation models. *J. Atmos. Sci.*, **33**, 405–412.

CLIMAP Project Members, 1976: The surface of the Ice-Age Earth. *Science*, **191**, 1131–1136.

——, 1981: Seasonal reconstructions of the earth's surface at the last glacial maximum. *Geol. Soc. Amer. Map Chart Ser.*, MC-36.

Denton, G. H., and T. J. Hughes, Eds., 1981: *The Last Great Ice Sheets.* Wiley, 484 pp., 28 folded maps.

Gates, W. L., 1976a: Modeling the ice-age climate. *Science*, **191**, 1138–1144.

——, 1976b: The numerical simulation of ice-age climate with a global general circulation model. *J. Atmos. Sci.*, **33**, 1844–1873.

Hansen, J., A. Lacis, D. Rind, G. Russell, P. Stone, I. Fung, R. Ruedy and J. Lerner, 1984: Climate sensitivity: Analysis of feedback mechanisms. *Climate Processes and Climate Sensitivity*, J. E. Hansen and T. Takahashi, Eds., Amer. Geophys. Union, Maurice Ewing Ser. No. 5, 130–163.

Hays, J. D., J. Imbrie and N. J. Shackleton, 1976: Variations in the Earth's orbit: Pacemaker of the ice ages. *Science*, **194**, 1121–1132.

Imbrie, J., and K. P. Imbrie, 1979: *Ice Ages: Solving the Mystery.* Enslow, 224 pp.

——, and J. Z. Imbrie, 1980: Modeling the climatic response to orbital variations. *Science*, **207**, 943–953.

Kellog, W. W., 1978: Global influences of mankind on the climate. *Climatic Change*, J. Gribbin, Ed., Cambridge University Press, 205–227.

Kolla, V., P. E. Biscaye and A. F. Hanley, 1979: Distribution of quartz in late Quaternary Atlantic sediments in relation to climate. *Quat. Res.*, **11**, 261–277.

Kutzbach, J. E., 1981: Monsoon climate of the early Holocene: Climatic experiment using the Earth's orbital parameters for 9000 years ago. *Science*, **214**, 59–61.

——, 1983: Monsoon rains of the late Pleistocene and early Holocene: Patterns, intensity and possible causes of changes. *Variations in the Global Water Budget*, F. A. Street-Perrott et al., Eds., Reidel, pp. 371–389.

——, and Otto-Bliesner, 1982: The sensitivity of the African-Asian monsoonal climate to orbital parameter changes for 9000 years B.P. in a low-resolution general circulation model. *J. Atmos. Sci.*, **39**, 1177–1188.

——, and P. J. Guetter, 1984a: Sensitivity of late glacial and Holocene climates to the combined effects of orbital parameter changes and lower boundary condition changes: "Snapshot" simulations with a general circulation model for 18, 9, and 6 kyr BP. *Ann. Glaciol.*, **5**, 85–87.

——, and ——, 1984b: The sensitivity of monsoon climates to orbital parameter changes for 9000 years BP: Experiments with the NCAR general circulation model. *Milankovitch and Climate, Part 2*, A. Berger, J. Imbrie, J. Hays, G. Kukla and B. Saltzman, Eds., Reidel, 801–820.

——, and F. A. Street-Perrott, 1985: Milankovitch forcing of fluctuations in the level of tropical lakes from 18 to 0 kyr BP. *Nature*, **317**, 130–134.

——, and H. E. Wright, Jr., 1985: Simulation of the climate of 18,000 yr BP: results for the North American/North Atlantic/European Sector. *Quat. Sci. Rev.*, **4**, 147–187.

Lorius, C., D. Raynaud, J-R. Petit, J. Jousel and L. Merlivat, 1984: Late-glacial maximum-Holocene atmospheric and ice-thickness changes from Antarctic ice-core studies. *Ann. Glaciol.*, **5**, 88–94.

Manabe, S., and D. G. Hahn, 1977: Simulation of the tropical climate of an ice age. *J. Geophys. Res.*, **82**, 3889–3911.

——, and A. J. Broccoli, 1985: The influence of continental ice sheets on the climate of an ice age. *J. Geophys. Res.*, **90**, 2167–2190.

Milankovitch, M., 1941: Canon of insolation and the ice-age problem. *K. Serb. Akad. Geogr.*, Spec. Publ. No. 132, 484 pp. [Translated by Israel Program for Scientific Translations, Jerusalem, 1969, U.S. Dept. of Commerce.]

Mitchell, J. F. B., 1977: The effect on climate of changing the earth's orbital parameters; two summer integrations with fixed sea surface temperatures. Tech. Note, 11/100, 18, Meteorological Office 20, Bracknell, U.K.

Neftel, A., H. Oeschger, J. Schwander, B. Stauffer and R. Zumbrunn, 1982: Ice core sample measurements give atmospheric CO_2 content during the past 40 000 yr. *Nature*, **295**, 220–223.

North, G. R., J. G. Mengel and D. A. Short, 1983: A simple energy balance model resolving the seasons and the continents: Application to the astronomical theory of the ice ages. *J. Geophys. Res.*, **88**, 6576–6586.

Oeschger, H., J. Beer, V. Seigenthaler, B. Stauffer, W. Dansgaard and C. C. Langway, 1983: Late-glacial climate history from ice cores. *Paleoclimatic Models and Research*, A. Ghazi, Ed., Reidel, 95–107.

Peterson, G. M., T. Webb III, J. E. Kutzbach, T. Van der Hammen, T. A. Wijmstra and F. A. Street, 1979: The continental record of environmental conditions at 18 000 yr BP—an evaluation. *Quat. Res.*, **12**, 47–82.

Petit, J-R., M. Briat and A. Royer, 1981: Ice age aerosol content from East Antarctic ice core samples and past wind strength. *Nature*, **293**, 391–394.

Pitcher, E. J., R. C. Malone, V. Ramanathan, M. L. Blackmon, K. Puri and W. Bourke, 1983: January and July simulations with a spectral general circulation model. *J. Atmos. Sci.*, **40**, 580–604.

Porter, S. C., 1981: Glaciological evidence of Holocene climatic change. *Climate and History*, T. M. L. Wigley, M. J. Ingram and G. Farmer, Eds., Cambridge University Press, pp. 82–110.

Prell, W. L., 1978: *Evolution des Atmospheres Paletaives et Climatolgie de la Terre.* Centre National d'Etudes Spatiales, 149–156.

——, 1984: Monsoonal climate of the Arabian Sea during the Late Quaternary: A response to changing solar radiation. *Milankovitch and Climate, Part 1*, A. Berger, J. Imbrie, J. Hays, G. Kukla and B. Saltzman, Eds., Reidel, 349–366.

Ramanathan, V., 1981: The role of ocean-atmosphere interactions in the CO_2 climate problem. *J. Atmos. Sci.*, **38**, 918–930.

——, E. J. Pitcher, R. C. Malone and M. L. Blackmon, 1983: The response of a spectral general circulation model to refinements in radiative processes. *J. Atmos. Sci.*, **40**, 605–630.

Rind, D., and D. Peteet, 1985: Terrestrial conditions at the last glacial maximum and CLIMAP sea-surface temperature estimates: Are they consistent? *Quat. Res.*, **24**, 1–22.

Ruddiman, W. F., 1981: The North Atlantic Ocean during the last deglaciation. *Palaeogeogr., Palaeoclimatol., Palaeoecol.*, **35**, 145–214.

——, and A. McIntyre, 1981: Oceanic mechanisms for amplification of the 23,000-year ice-volume cycle. *Science*, **212**, 617–627.

——, and J.-C. Duplessy, 1985: Conference on the last deglaciation: Timing and mechanism. *Quat. Res.*, **23**, 1–17.

Schneider, S. H., and C. Mass, 1975: Volcanic dust, sunspots, and temperature trends. *Science*, **190**, 741–746.

——, and S. L. Thompson, 1979: Ice ages and orbital variations: Some simple theory and modeling. *Quat. Res.*, **12**, 188–203.

Street, F. A., and A. T. Grove, 1979: Global maps of lake-level fluctuations since 30,000 yr B.P. *Quat. Res.*, **12**, 83–118.

Street-Perrott, F. A., and N. Roberts, 1983: Fluctuations in closed-basin lakes as an indicator of past atmospheric circulation pat-

terns. *Variations in the Global Water Budget,* F. A. Street-Perrott, M. A. Beran and R. A. S. Ratcliffe, Eds., Reidel, pp. 331–345.

Stuiver, M., R. L. Burk and P. D. Quay, 1984: $^{13}C/^{12}C$ ratios in tree rings and the transfer of biospheric carbon to the atmosphere. *J. Geophys. Res.,* **89,** 11 734–11 748.

Suarez, M. J., and I. M. Held, 1976: Modeling climatic response to orbital parameter variations. *Nature,* **263,** 46–47.

Thompson, L. G., and E. Mosley-Thompson, 1981: Temporal variability of microparticle properties in polar ice sheets. *J. Volc. Geotherm. Res.,* **11,** 11–27.

Vernekar, A. D., 1972: *Long-period Global Variations of Incoming Solar Radiation. Meteor. Monogr.,* No. 34, Amer. Meteor. Soc., 9 pp.

Washington, W. M., and G. A. Meehl, 1984: Seasonal cycle experiment on the climate sensitivity due to a doubling of CO_2 with an atmospheric general circulation model coupled to a simple mixed-layer ocean model. *J. Geophys. Res.,* **89,** 9475–9503.

Webb, T. III, 1985: A global paleoclimatic data base for 6000 yr B.P. Dept. of Energy, Carbon Dioxide Research Division Rep. TRO 18 (DOE/EV/10097-6), Washington, DC, 155 pp. [Available from the NTIS, U.S. Dept. of Commerce, Springfield, VA 22161.]

——, E. J. Cushing and H. E. Wright, Jr., 1983: Holocene changes in the vegetation of the Midwest. *Late Quaternary Environments of the United States, Vol. 2: The Holocene,* H. E. Wright, Jr., Ed., University of Minnesota Press, 142–165.

——, J. Kutzbach and F. A. Street-Perrott, 1985: 20,000 years of global climatic change: Paleoclimatic research plan. *Global Change,* T. F. Malone and J. G. Roeder, Eds., ICSU Press, 182–218.

Wetherald, R. T., and S. Manabe, 1975: The effects of changing the solar constant on the climate of a general circulation model. *J. Atmos. Sci.,* **32,** 2044–2059.

Williams, J., R. G. Barry and W. W. Washington, 1974: Simulation of the atmospheric circulation using the NCAR global circulation model with ice age boundary conditions. *J. Appl. Meteor.,* **13,** 305–317.

Wright, H. E., Jr., 1971: Late Quaternary vegetation history of North America. *The Late Cenozoic Ice Ages,* K. Turekian, Ed., Yale University Press, 425–464.